Received 21 November 2022; revised 16 December 2022; accepted 20 December 2022. Date of publication 30 December 2022; date of current version 17 January 2023.

Digital Object Identifier 10.1109/OJCOMS.2022.3232279

Sensing Using Coded Communications Signals

SUNDAR ADITYA [1] (Member, IEEE), ONUR DIZDAR [1,2] (Member, IEEE), BRUNO CLERCKX [1,3] (Fellow, IEEE), AND XUERU LI [4] (Member, IEEE)

[1]Department of Electrical and Electronic Engineering, Imperial College London, SW7 2AZ London, U.K.

[2]Research and Technology Group, Viavi Solutions UK Ltd., SG1 2AN Stevenage, U.K.

[3]Silicon Austria Labs, 8010 Graz, Austria

[4]Huawei Device Company Ltd., Shenzhen 518108, China

CORRESPONDING AUTHOR: S. ADITYA (e-mail: s.aditya@imperial.ac.uk).

This work was supported by the Huawei Device Company Ltd.

ABSTRACT A key challenge for common waveforms for Integrated Sensing and Communications – widely regarded as a resource-efficient way to achieve high performance for both functionalities – lies in leveraging information-bearing channel-coded communications signal(s) (c.c.s) for sensing. In this paper, we investigate the range-Doppler sensing performance of c.c.s in multi-user interference-limited scenarios, and show that it is affected by *sidelobes* whose form depends on whether the c.c.s modulates a single-carrier or OFDM waveform. While uncoded signals give rise to *asymptotically zero sidelobes* due to the law of large numbers, it is not obvious that the same holds for c.c.s, as structured codes (e.g., linear block codes) induce dependence across codeword symbols. In this paper, we show that c.c.s also give rise to asymptotically zero sidelobes – for both single-carrier and OFDM waveforms – by deriving upper bounds for the tail probabilities of the sidelobe magnitudes that decay as $\exp(-O(\text{code rate} \times \text{block length}))$. Consequently, for any code rate, c.c.s are effective sensing signals that are robust to multi-user interference at *sufficiently large* block lengths, with negligible difference in performance based on whether they modulate a single-carrier or OFDM waveform. We verify the latter implication through simulations, where we observe the sensing performance (i.e., the detection and false-alarm probabilities) of a QPSK-modulated c.c.s (code rate $= 120/1024$, block length $= 1024$ symbols) to match that of a comparable interference-free FMCW waveform even at high interference levels (SIR of -11dB), for both single-carrier and OFDM waveforms.

INDEX TERMS Correlation properties of coded communications signals (c.c.s), integrated sensing and communications (ISAC), interference sidelobes, opportunistic sensing, sensing in beyond 5G networks, sensing interference management.

I. INTRODUCTION

A COMBINATION of factors, such as (a) supporting emerging applications that require both communications and sensing functionalities (e.g., augmented/virtual reality, autonomous vehicles, etc.) in beyond 5G networks, and (b) the channel propagation characteristics at mmWave and THz frequency bands, have provided the impetus for ongoing research efforts on integrated sensing and communications (ISAC). In this regard, the waveform used for each of the functionalities is a crucial aspect of system design. Broadly, there are two paradigms of waveform design for ISAC systems (see [1] for a comprehensive survey):

a) *Separate waveforms*: Such an approach allows commercial stakeholders, who may have expertise in either communications or sensing but not both, to continue to independently design their hardware and systems, based on the desirable waveform properties for each functionality (e.g., FMCW for radar and OFDM for communications). The individual waveforms can either

be transmitted orthogonally [2], [3] or superimposed [4], [5], [6], [7], provided the mutual interference is effectively mitigated.

b) *Common waveform*: The efficient utilization of valuable spectral, hardware and energy resources is the driving factor behind this approach [8], with [9], [10], [11] being good examples of optimizing resource allocation (e.g., power, subcarriers etc.) between communications and sensing for a common OFDM waveform. In contrast to these, a special case of a common waveform involves using *only* the reference signals of a primarily communications waveform, such as IEEE 802.11ad frames, for sensing [12], [13], [14], [15]. Such a solution has the advantage of not requiring extensive standardization efforts; however, it is sub-optimal as, in principle, even the communications payload/signal can be used for sensing in a monostatic configuration (i.e., where the transmitter and receiver are collocated), since it is known apriori at the transmitting node.

In this paper, we explore the *range-Doppler* sensing potential of (channel) coded communications signals (c.c.s) – i.e., the communications payload – when embedded in a common ISAC waveform. A key question w.r.t a common ISAC waveform is whether to adopt a single- or multi-carrier waveform. Most discussion on the benefits of one waveform over the other focus on issues like signal processing complexity (both communications and sensing), easy integration with existing standards, PAPR etc. [16], [17]. Our focus on the single- versus multi-carrier question in this paper is restricted to the impact, if any, of channel coding on the range-Doppler sensing performance of each waveform, especially in interference-limited environments. We show that for any code rate, c.c.s are effective sensing signals that are robust to multi-user interference at *sufficiently large* block lengths, with negligible difference in performance based on whether they modulate a single-carrier or OFDM waveform.

RELATED WORK

Sensing (e.g., radar) is typically modeled as estimating a target's range, velocity (Doppler) and angular coordinates. Since MIMO is a cornerstone of modern communications, many papers on ISAC focus on the integration of MIMO communications with MIMO radar through a common transmit waveform [18], [19], [20], [21], [22], [23]. In these papers, the sensing task is implicitly assumed to be target direction-finding, where for sufficiently large SNR, the achievable angular resolution is determined by the array aperture. Importantly, the time-frequency characteristics of the sensing signal do not influence the angular sensing performance. Consequently, such papers *rightly* assume that beamformed communications signals from MIMO communications can be used to realize (angular) sensing objectives like beampattern optimization, as well.

Our focus however is on range-Doppler sensing, where the time-frequency characteristics of the sensing signal do influence the sensing performance. Several papers have investigated ISAC waveform design with range-Doppler sensing in mind [24], [25], [26], [27]. Among these, [24], [25], [26] modify a *primarily* radar waveform to also carry communications symbols, while [27] uses sparsity to realize an ambiguity function with low sidelobes from a communications data stream. A common theme among these solutions is a lower communications spectral efficiency (bits/channel use), which is at odds with the higher spectral efficiencies targeted for next-generation wireless networks [28]. Thus, the goal of simultaneously supporting higher data rates and sensing functionality using a common waveform motivates us to investigate the sensing performance of a *primarily* communications waveform, especially its data payload.

The principle of using known data symbols for monostatic range-Doppler sensing has been explored for a variety of candidate waveforms, such as single-carrier [23], [29], [30], OFDM [9], [31], [32], [33], [34], and OTFS (Orthogonal Time Frequency and Space) [35]. Among these, [9], [31] and [35] consider uncoded communications signals, while [23], [30] assume that the communications symbols are drawn from a Gaussian distribution. Neither of these models are representative of typical data payloads that are subject to channel coding. The assumptions around channel coding in [29], [32] and [33] are unclear and the latter two references, in particular, are experimental studies exploring the sensing potential of 5G NR signals. Hence, even if channel coding was implied, its impact on the sensing performance was not investigated. Finally, none of the above references addresses the impact of interference on the sensing performance of c.c.s.

MOTIVATION

To motivate the discussion on the sensing potential of c.c.s in interference-limited operating environments, consider the scenario in Fig. 1a, where TX i communicates with RX i ($i = 1, \ldots, M_r$), while all the TXs also act as monostatic radars to simultaneously sense a scene without cooperation. Each TX/radar realizes communications and sensing using a common ISAC waveform. Such a setup gives rise to *multi-user* communications and sensing interference (highlighted in Fig. 1a). The former is the interference experienced at RX i due to the transmissions of TX $j(\neq i)$, while the latter is the interference at radar receiver i (collocated with TX i) due to the transmissions of TX/radar $j(\neq i)$.[1] In general, the two types of interference are distinct in their profiles, and we are especially interested in cases where the sensing interference *dominates* the communications interference. An example of such a scenario could occur in a vehicular network, as depicted in Fig. 1b, where a pair of vehicular TXs/radars (i.e., $M_r = 2$) are facing each other on opposite lanes and sensing the road ahead of them, while also communicating with their respective RXs, which may be nearby road side units (RSUs) on

1. Note that our definition of multi-user sensing interference is distinct from adversarial interference like jamming, which we do not consider in this paper. For brevity, we drop the 'multi-user' prefix when discussing sensing interference from here on.

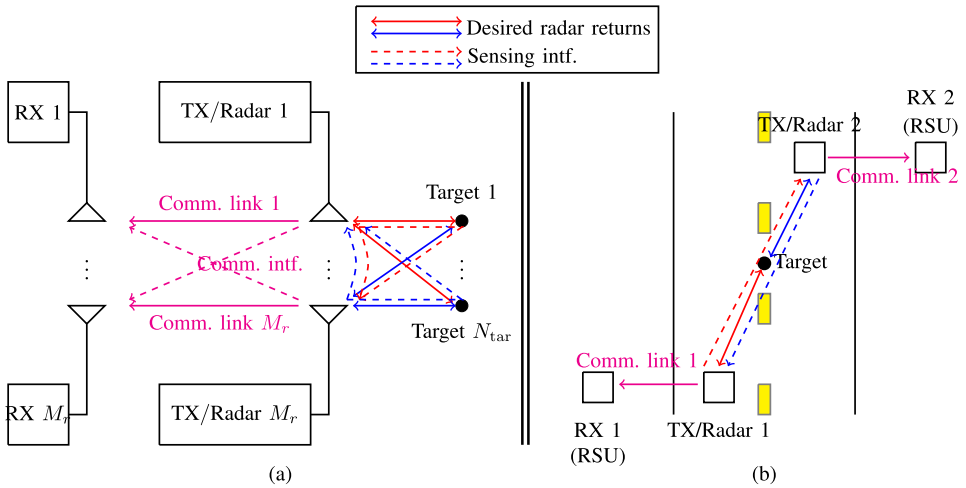

FIGURE 1. (a) Using a common transmit waveform, TX i communicates with RX i ($i = 1, \ldots, M_r$), while all TXs/radars simultaneously sense a common target scene non-cooperatively. This gives rise to distinct communications and sensing interference, where the latter often dominates the former due to a combination of link geometry and/or greater pathloss experienced by the desired radar returns; e.g., in (b) a vehicular network that can be interpreted as a special case of (a), corresponding to $M_r = 2$ and $N_{\text{tar}} = 1$.

the sidewalk. The geometry of this scene is such that despite narrow beams enabled by large antenna arrays, beamforming may only be able to suppress communications – but not *sensing* – interference, as there could still be significant signal leakage along the direct (line-of-sight) path linking the two TXs. Geometry apart, an R^{-4} attenuation of the desired radar returns – in contrast to the R^{-2} attenuation for the interference signal along the direct path between two radars – also makes it more likely that sensing interference dominates communications interference in other ISAC use cases. Hence, at first glance, it is tempting to allocate the available communications resources (e.g., time and frequency bands) orthogonally across TXs to mitigate the sensing interference at the expense of communications spectral efficiency (measured in bits/s/Hz). However, if c.c.s happen to be *good* sensing signals – meaning, achieving high sensing performance, while being robust to sensing interference – then, the communications spectral efficiency in Fig. 1 can be significantly enhanced through a reuse factor of one.

To provide intuition for why communications signals might be good sensing signals, consider a collection of M_r *uncoded* communications signals – $\{v^{(i)}[n] : n = 0, \ldots, N-1;\ i = 1, \ldots, M_r\}$ – comprising i.i.d zero mean, unit-energy symbols (e.g., QPSK). From the law of large numbers (LLN), it can easily be shown that these signals have *asymptotically favourable correlation properties* (i.e., auto-correlation function tending to the δ-function, and mutual cross-correlation function tending to the zero function, as $N \to \infty$), which – as shown in Section II-B1 – makes them good sensing signals, when embedded in a single-carrier waveform. Similarly, the IDFT of $v^{(q)}[n]/v^{(i)}[n]$ $(q \neq i)$ identically tends to 0, as $N \to \infty$, which – as shown in Section II-B2 – makes the collection of signals $\{v^{(i)}[n]: i = 1, \ldots, M_r\}$ robust to sensing interference, when embedded in an OFDM waveform. However, structured state-of-the-art channel coding schemes (e.g., linear block codes, such as Polar and LDPC codes) induce statistical dependence across bits/symbols, which means that LLN can no longer be applied in a straightforward manner to characterize the behavior of the above functions of c.c.s. To the best of our knowledge, the impact of statistical dependence across symbols on the sensing performance of c.c.s has not been investigated in the literature, and we seek to fill this gap with a view to determine if (a) c.c.s can indeed achieve high sensing performance, while being robust to sensing interference, and (b) whether the nature of the waveform (i.e., single- v/s multi-carrier) influences the answer to (a). Our contributions are as follows:

1. *Single-Carrier Waveform:*
   (i) We derive an upper bound for the tail probability of (the non-zero lags of) the auto-correlation function of c.c.s that decays as $\exp(-O(rN))$, where r is the code rate and N is the block length (Theorem 1). Consequently, c.c.s have an *asymptotically ideal* auto-correlation function that converges in distribution to (a suitably scaled) δ-function for large block lengths (Corollary 1). Hence, c.c.s are good sensing signals when embedded in a single-carrier waveform. These results makes mild assumptions regarding c.c.s and importantly, do not depend on the code structure.
   (ii) For a pair of c.c.s with rates r_i and r_q, generated from independent message signals, we derive an upper bound for the tail probability of their cross-correlation function that decays as $\exp(-O(\max(r_i, r_q)N))$ (Corollary 2). Consequently, c.c.s generated by independent message signals have a cross-correlation function that converges in distribution to the zero function for large block lengths (Corollary 4). Hence, c.c.s are robust to sensing interference, when embedded in a single-carrier waveform.

(iii) For linear codes, we derive lower bounds for the tail probabilities of the auto- and cross-correlation functions of c.c.s that also decay as $\exp(-O(rN))$ (Theorem 2 and Corollary 3, respectively). These results, along with the previous bullet points, imply that for linear codes, a faster order of decay for these functions, as a function of N, is not possible.

2. *OFDM Waveform:*
   (i) For a pair of c.c.s, $s^{(i)}[n]$ and $s^{(q)}[n]$, with rates r_i and r_q, respectively,generated from independent message signals, we derive an upper bound for the tail probability of the IDFT of $s^{(q)}[n]/s^{(i)}[n]$ that decays as $\exp(-O(\min(r_i, r_q)N)$ (Corollary 5). As a result, the above IDFT converges in distribution to the zero function for large block lengths (Corollary 7). Hence, c.c.s are robust to sensing interference, when embedded in an OFDM waveform.
   (ii) For the same setup as the previous bullet point, but with linear codes, we derive a lower bound for the tail probability of the IDFT of $s^{(q)}[n]/s^{(i)}[n]$, that decays as $\exp(-O((r_i + r_q)N))$ (Corollary 6). The latter result, along with the one from the previous bullet point, implies that for linear codes, a faster order of decay for the IDFT in question, as a function of N, is not possible.
3. *Implications:*
   (i) The results under points 1 and 2 above suggest that for any code rate, c.c.s can be effective sensing signals that are robust to sensing interference at *sufficiently large* block lengths. Furthermore, any performance difference based on whether the c.c.s modulate a single-carrier or OFDM waveform is expected to be negligible in the large block regime. We verify these implications through simulations, where we observe that the sensing performance (characterized by the detection and false-alarm probabilities) of a QPSK-modulated c.c.s (code rate $= 120/1024$, block length $= 1024$ symbols) matches that of a comparable interference-free FMCW waveform even at a signal-to-interference ratio (SIR) of -11dB, for both single-carrier and OFDM waveforms.
   (ii) Thus, a common ISAC waveform (either single- or multi-carrier, but) largely comprising coded data symbols is an effective sensing signal at large block lengths that can also achieve high communications spectral efficiency. Moreover, in multi-user ISAC scenarios with such a waveform, sensing interference management essentially *takes care of itself* for monostatic radars, and is relatively simpler than communications interference management. Such a result is favourable for the evolution of existing wireless broadband networks to support sensing applications.

This paper consists of five sections. In our system model in Section II, we identify functions of c.c.s – depending on whether they modulate a single-carrier or OFDM waveform – whose tail distribution needs to decay rapidly for c.c.s to be good sensing signals. In Section III, we characterize the tail probabilities of these functions and show that they decay rapidly at large block lengths. We verify the effectiveness of c.c.s as sensing signals in interference-limited environments through simulations in Section IV, where we see that the sensing performance of c.c.s – for both single-carrier and OFDM waveforms – is at par with the (interference-free) FMCW waveform, even at a SIR of -11dB. Finally, we conclude this paper in Section V with some remarks on the implications of our results.

NOTATION

Vectors are represented by lower case bold letters (e.g., $\mathbf{a}$); $\mathcal{CN}(0, \sigma^2)$ denotes the circularly symmetric complex Gaussian distribution with mean zero and variance σ^2; $\delta[\cdot]$ and $\mathbb{1}(\cdot)$ denote the discrete delta and the indicator functions, respectively; $\mathbb{P}(\cdot)$ denotes probability; $\mathbb{E}[\cdot]$ denotes the expectation operator; $(\cdot)^*$ denotes complex conjugation, and $\Re\{\cdot\}$ denotes the real part. We assume that all discrete-time signals are supported on $\mathbb{Z}$, the set of integers, with the understanding that for a signal, $s[n]$ $(n = 0, \ldots, N-1)$, with finite support, $s[n] = 0$ for $n \notin \{0, \ldots, N-1\}$. Finally, we introduce a few definitions that will be used throughout the paper:

Definition 1 (Auto-Correlation Function): For a discrete-time signal, $s[n]$ $(n = 0, \ldots, N-1)$, its (aperiodic) auto-correlation function at lag $l \in \mathbb{Z}$, denoted by $\chi(l; s[\cdot])$, is given by:

$$\chi(l; s[\cdot]) \coloneqq \frac{1}{N} \sum_{n=-\infty}^{\infty} s[n]s^*[n-l]. \tag{1}$$

Definition 2 (Cross-Correlation Function): For a pair of signals, $s_1[n]$ and $s_2[n]$ $(n = 0, \ldots, N-1)$, their (aperiodic) cross-correlation function at lag $l \in \mathbb{Z}$, denoted by $\varrho(l; s_1[\cdot], s_2[\cdot])$, is given by:

$$\varrho(l; s_1[\cdot], s_2[\cdot]) \coloneqq \frac{1}{N} \sum_{n=-\infty}^{\infty} s_1[n]s_2^*[n-l]. \tag{2}$$

Clearly, by definition, $\chi(l; s[\cdot]) = \varrho(l; s_1[\cdot], s_2[\cdot]) = 0$ for $|l| \geq N$. Hence, in this paper, we focus on the behavior of $\chi(l; s[\cdot])$ and $\varrho(l; s_1[\cdot], s_2[\cdot])$ for $|l| \ll N$, for large N. Alternately, for N-length signals, periodic auto- and cross-correlation functions can be defined by replacing the term $n - l$ with $(n - l) \mod N$ in (1) and (2), respectively. Our results in this paper are valid for these functions, as well.

Definition 3 (Convergence in Distribution): A sequence of random variables, $X_1, \ldots, X_n$ converges in distribution to a random variable, X – denoted by $\lim_{n\to\infty} X_n \xrightarrow{d} X$ – if the following condition is satisfied:

$$\lim_{n\to\infty} \mathbb{P}(X_n > u) = \mathbb{P}(X > u), \tag{3}$$

for all u where the tail distribution, $\mathbb{P}(X > u)$, is continuous.

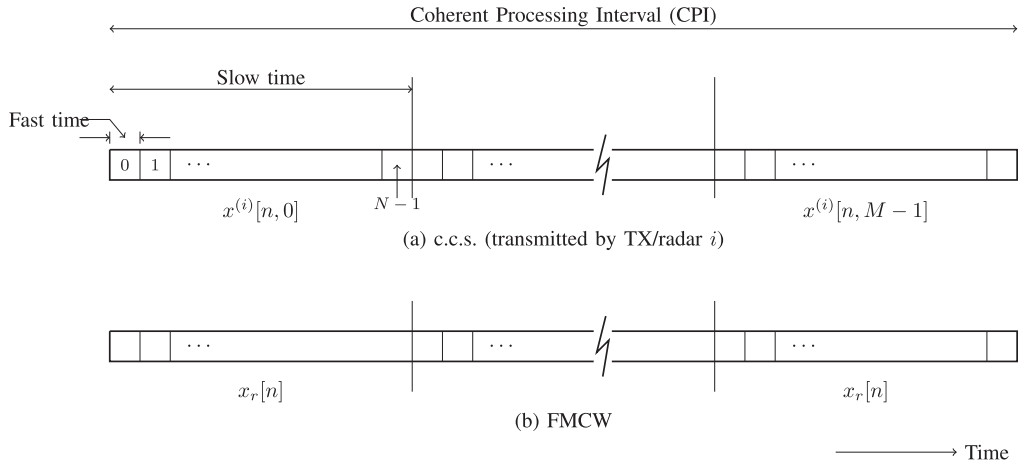

FIGURE 2. Sensing signal structure in (discrete) time-domain for range-Doppler estimation.

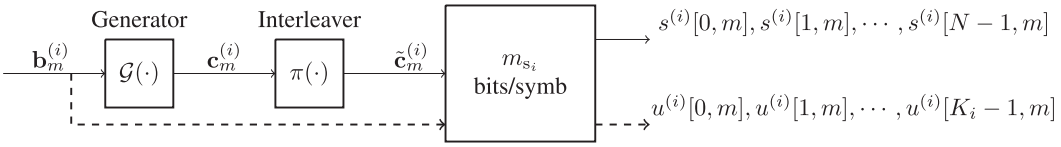

FIGURE 3. BICM model for a complex-valued c.c.s, that determines the signal $x^{(i)}[n, m]$ transmitted by the i-th TX/radar in Fig. 2a in the m-th slow time interval.

II. SYSTEM MODEL

Consider the scenario in Fig. 1a, where TX i communicates with RX i $(= 1, \ldots, M_r)$, while all the TXs also act as monostatic radars to simultaneously sense a scene comprising N_{tar} targets without cooperation. Let $\mathcal{X}_{M,N}^{(i)} \coloneqq \{x^{(i)}[n,m] \in \mathbb{C}\colon\ m = 0, \ldots, M-1;\ \ n = 0, \ldots, N-1\}$ denote the (discrete) time-domain representation of the common ISAC waveform transmitted by the i-th TX/radar, which can be interpreted as a collection of M signals, each of length N – i.e., $\{x^{(i)}[n,0], \ldots, x^{(i)}[n,M-1]\colon n = 0, \ldots, N-1\}$ – where $x^{(i)}[n,0]$ is transmitted first, followed by $x^{(i)}[n,1]$, and so on, as shown in Fig. 2a.[2] The indices, n and m, represent two different timescales under the assumption that the timescale associated with range resolution (i.e., n, also known as *fast time*) is far smaller than the timescale over which the Doppler frequencies associated with moving targets shows an appreciable change in phase (i.e., m, also known as *slow time*). This is a common assumption in many radar applications (e.g., automotive radar) and its validity is discussed later in Remark 1. In general, for fixed m, each signal $x^{(i)}[n,m]$ is a function of a c.c.s, $s^{(i)}[n,m]$, whose modeling is described below.

A. C.C.S MODEL

We consider a BICM (Bit Interleaved Coded Modulation) model for c.c.s as shown in Fig. 3. At TX i, for each m, a binary message vector, $\mathbf{b}_m^{(i)} \in \{0,1\}^{K_i m_{s_i}}$, of length $K_i m_{s_i}$ is transformed into a binary codeword vector, $\mathbf{c}_m^{(i)} \in \{0,1\}^{N m_{s_i}}$, of length $N m_{s_i}$ through a generator mapping, $\mathcal{G}(\cdot)$.[3] The encoded bits – which are statistically dependent, in general – are then interleaved and mapped to a discrete, bounded constellation through a mapping that associates m_{s_i} bits per symbol to produce a complex-valued c.c.s block, $s^{(i)}[n,m]$ $(n = 0, \ldots, N-1)$, of block length,[4] N. Importantly, interleaving and modulation do not produce i.i.d symbols, in general.

Let $u^{(i)}[n,m]$ $(n = 0, \ldots, K_i - 1)$ denote the complex-valued message signal, of length K_i, obtained by mapping $\mathbf{b}_m^{(i)}$ to the same constellation. Thus, the code rate, r_i, of $s^{(i)}[n,m]$ equals K_i/N. In general, each c.c.s symbol, $s^{(i)}[n,m]$, is a *non-linear* function of one or more message symbols ($u^{(i)}[n_1,m]$, $u^{(i)}[n_2,m]$, …, etc.), which is difficult to characterize for most modulation and coding schemes.[5] Thus, for tractability, we make some assumptions regarding the signals $u^{(i)}[n,m]$ and $s^{(i)}[n,m]$ below.

Assumption 1 (i.i.d. Zero-Mean Message Symbols): The message symbols, $u^{(i)}[0,m], \ldots, u^{(i)}[K_i-1,m]$ are i.i.d with zero mean and finite energy, as they are typically drawn uniformly from bounded, symmetric constellations like QPSK, QAM, etc.

2. Typically, in purely radar applications, $x^{(i)}[n,m]$ is identical $\forall m \in \{0, \ldots, M-1\}$ (e.g., Fig. 2b). However, this is not a strict requirement.

3. For linear block codes, $\mathcal{G}(\cdot)$ takes the form of a generator/parity-check matrix.

4. In coding theory, the block length typically refers to the number of bits in the codeword vector, $\mathbf{c}_m^{(i)}$ (equal to $N m_{s_i}$). Since the quantities of interest in this paper take values in $\mathbb{C}$ (e.g., the auto-correlation function), we slightly abuse the notation and refer to the number of complex-valued symbols in the signal $s^{(i)}[n,m]$ (for fixed m) as the block length.

5. Even for linear codes, the relationship between the message and c.c.s symbols is non-linear, due to the symbol mapping operation.

Assumption 2 (Systematic Encoding): The first K_i c.c.s symbols coincide with the message symbols, i.e., $s^{(i)}[n,m] = u^{(i)}[n,m]$ $(n = 0,\ldots,K_i-1)$. This is referred to as systematic encoding and any linear block code can be transformed into such a form through a linear mapping. Since widely used codes such as LDPC and Polar Codes are linear block codes, we believe the systematic encoding assumption[6] is reasonable.

Assumption 3 (Uncorrelated c.c.s Symbols): While the c.c.s symbols, $s^{(i)}[0,m],\ldots,s^{(i)}[N-1,m]$, are statistically dependent in general, we assume that they are mutually uncorrelated. While Assumption 2 ensures that the first K_i symbols are uncorrelated, the encoding operation typically introduces correlation across subsequent codeword bits (i.e., in $\mathbf{c}_m^{(i)}$ in Fig. 3), which can be mitigated by interleaving; for instance, in Appendix I, we demonstrate that for repetition codes,[7] the interleaved codeword bits ($\tilde{\mathbf{c}}_m^{(i)}$ in Fig. 3) are asymptotically uncorrelated for large N (i.e., the correlation coefficient between a pair of arbitrarily chosen bits in $\tilde{\mathbf{c}}_m^{(i)}$ tends to 0, as $N\to\infty$). Hence, with interleaving, we believe uncorrelated c.c.s symbols is a reasonable assumption for most practical codes.

The relationship between the signals $s^{(i)}[n,m]$ and $x^{(i)}[n,m]$ depends on whether the latter is a single- or multi-carrier waveform. We characterize this relationship for a representative of each type, namely the conventional single-carrier and the OFDM waveforms.

1) CONVENTIONAL SINGLE-CARRIER

The c.c.s symbols are transmitted as is in (discrete) time-domain, i.e.,

$$x^{(i)}[n,m] = s^{(i)}[n,m]. \tag{4}$$

2) OFDM

The c.c.s symbols in $s^{(i)}[k,m]$ $(k=0,\ldots,N-1)$ are multiplexed in the frequency domain over N subcarriers to constitute the m-th OFDM symbol. Thus, $x^{(i)}[n,m]$ and $s^{(i)}[k,m]$ are related by an IDFT, as follows:

$$x^{(i)}[n,m] = \frac{1}{N}\sum_{k=0}^{N-1} s^{(i)}[k,m]\exp\left(j2\pi\frac{n}{N}k\right). \tag{5}$$

The total number of OFDM symbols transmitted equals M, as per Fig. 2a.

B. SENSING MODEL

For the target scene in Fig. 1a, let $(n_t^{(i)}, m_t^{(i)})$ denote the (range, Doppler)-bin[8] in which the t-th target $(t = 1,\ldots,N_{\text{tar}})$ is situated w.r.t the i-th TX/radar. In other words, $(n_t^{(i)}, m_t^{(i)}) \in \{1,\ldots,n_{\max}\}\times\{1,\ldots,M\}$ corresponds to the path TX $i\to$ Target $\to$ TX i, where $n_{\max} \ll N$ denotes the range bin associated with the maximum detectable range. Assuming no carrier frequency offset[9] and sufficient self-interference suppression, the (discrete) time-domain radar return, $y^{(i)}[n,m]$, at the i-th TX/radar corresponding to the transmitted signal $x^{(i)}[n,m]$ is given by:

$$y^{(i)}[n,m] = \underbrace{\sum_{t=1}^{N_{\text{tar}}} \alpha_t^{(i)} x^{(i)}[n-n_t^{(i)},m]\exp\left(j2\pi\frac{m_t^{(i)}}{M}m\right)}_{\text{Desired radar returns}} + \underbrace{y_{\text{intf}}^{(i)}[n,m]}_{\text{Sensing intf.}} + w^{(i)}[n,m], \tag{6}$$

where

- $\alpha_t^{(i)} \in \mathbb{C}$ is the gain, capturing the combined effects of beamforming, path loss, and target reflection/scattering along the path TX $i\to$ Target $t\to$ TX i;
- $y_{\text{intf}}^{(i)}[n,m]$ denotes the *sensing interference* signal at the i-th TX/radar; and,
- $w^{(i)}[n,m] \sim \mathcal{CN}(0,\sigma^2)$ is the additive noise signal, independent of the radar returns, and also across n,m.

Remark 1 (Range-Doppler Decoupling): In the terms capturing the desired radar returns in (6), the delay shift corresponding to the target ranges is assumed to be the same across all m, and the Doppler shift corresponding to the target velocities is assumed to be constant over the duration of a slow-time interval (m). Such a decoupling across the two timescales, n and m, can be assumed when the Doppler frequency is much smaller than the signal bandwidth.[10]

We model $y_{\text{intf}}^{(i)}[n,m]$ as follows: let $y_{\text{intf}}^{(q\to i)}[n,m]$ denote the sensing interference experienced at the i-th TX/radar due to the transmissions of TX/radar q $(\neq i)$, which can be expressed as a superposition of $N_{\text{tar}}+1$ components as follows:

$$y_{\text{intf}}^{(q\to i)}[n,m] = \sum_{l=0}^{N_{\text{tar}}} \alpha_l^{(q\to i)} x^{(q)}[n-n_l^{(q\to i)},m] \times \exp\left(j2\pi\frac{m_l^{(q\to i)}}{M}m\right). \tag{7}$$

The l-th term in (7) represents the interfering signal along the path TX $q\to$ Target $l\to$ TX i for $l\neq 0$, while the term corresponding to $l=0$ represents the signal leakage along the direct path TX $q\to$ TX i. Similar to the desired radar returns in (6), each such path is parameterized by a gain, delay and Doppler shift, captured by $\alpha_l^{(q\to i)}\in\mathbb{C}$, $n_l^{(q\to i)}\in$

6. Note that we assume systematic encoding post-interleaving, as illustrated in Fig. 3. Hence, $\pi(k) = k$ for $k\in\{1,\ldots,K_i m_{s_i}\}$, where $\pi(k)$ denotes the position of the k-th bit of $\mathbf{c}_m^{(i)}$ in the interleaved codeword, $\tilde{\mathbf{c}}_m^{(i)}$.

7. In a sense, the repetition code induces the "strongest" correlation across certain codeword bits/symbols.

8. A target at a distance d and moving at velocity v from the radar is said to be in range-Doppler bin (n_0,m_0) for n_0 and m_0 satisfying: $(n_0-1)\frac{c}{2B} \le d < n_0\frac{c}{2B}$, $(m_0-1)\frac{B}{MN} \le f_c\frac{2v}{c} < m_0\frac{B}{2MN}$, where c, B, and f_c denote the speed of light, bandwidth, and the carrier frequency, respectively.

9. This is a reasonable assumption for monostatic radars.

10. For a signal bandwidth $B = 1$GHz (enabling a range resolution of 15cm) and block length, $N = 1000$ symbols, the slow-time duration is $N/B = 1\mu$ s. At a carrier frequency of 100GHz, a target moving at 30mph yields a maximum Doppler frequency of $\approx$ 9kHz. The variation in the phase of a 9kHz sinusoid over 1μs is negligible.

$\{1, \ldots, n_{\max}\}$ and $m_l^{(q\to i)} \in \{1, \ldots, M\}$, respectively. Thus, $y_{\text{intf}}^{(i)}[n, m]$ can be expressed as follows:

$$y_{\text{intf}}^{(i)}[n, m] = \sum_{q \neq i} y_{\text{intf}}^{(q\to i)}[n, m]. \tag{8}$$

We now explore the sensing signal processing for conventional single-carrier and OFDM waveforms.

1) CONVENTIONAL SINGLE-CARRIER

For a single-carrier waveform, the target range bins can be estimated from (6) using a bank of matched filters, followed by a DFT to estimate the Doppler bins. Let $r^{(i)}[l, m]$ ($l = 1, \ldots, n_{\max}$) denote the (normalized) matched filter output, corresponding to $y^{(i)}[n, m]$ and $x^{(i)}[n, m]$, whose expression is given by (9), shown at the bottom of the page, which in turn, is obtained from (4) and Definitions 1 and 2.

Remark 2 (Sensing Interference Management for a Single-Carrier Waveform): The sensing interference in (9) can be completely eliminated if and only if the collection of c.c.s transmitted by the TXs have mutually zero cross-correlation across all lags [i.e., $\varrho(l; s^{(q)}[\cdot, m], s^{(i)}[\cdot, m]) \equiv 0,\ \forall q \neq i$], which is unlikely for all realizations of random c.c.s, $s^{(i)}[n, m]$ and $s^{(q)}[n, m]$. In particular, a large value of $|\varrho(l; s^{(i)}[\cdot, m], s^{(q)}[\cdot, m])|$ at a non-target range bin, l, gives rise to undesired sidelobes in $|r^{(i)}[l, m]|$ that affect the sensing performance by giving rise to false-alarms and missed detections – the latter due to the near-far effect, wherein the weaker peaks of farther targets are buried among the stronger interference sidelobes. To minimize the occurrence of these outcomes, it is desirable for $\mathbb{P}(|\varrho(l; s^{(i)}[\cdot, m], s^{(q)}[\cdot, m])| > u)$ – the tail probability of $|\varrho(l; s^{(i)}[\cdot, m], s^{(q)}[\cdot, m])|$ – to decay rapidly[11] w.r.t u. We characterize this quantity in terms of the c.c.s parameters (i.e., r_i, r_q and N) in Section III-B.

The single-carrier range-Doppler map, $R_{\text{sc}}^{(i)}[l, \nu]$, whose magnitude captures the strength of the radar return from the l-th range bin and ν-th Doppler bin, can be obtained from $r^{(i)}[l, m]$ through a M-point DFT across the slow time index, m.[12] Assuming the cross-correlation tail probabilities decay rapidly as per Remark 2 for the sensing interference terms in (9) to be negligible, the resulting expression for $R_{\text{sc}}^{(i)}[l, \nu]$ is given by (11), shown at the bottom of the page.

Remark 3 (Ideal Auto-Correlation): It is easy to see from (11) that at large enough SNR, if $\chi(l; s^{(i)}[\cdot, m]) \propto \delta[l]\ \forall m$ (i.e., the ideal auto-correlation function), then $R_{\text{sc}}^{(i)}[l, \nu] \propto \sum_{t=1}^{N_{\text{tar}}} \alpha_t^{(i)} \delta[l - n_t^{(i)}] \delta[\nu - m_t^{(i)}]$, resulting in sharp peaks for $|R_{\text{sc}}^{(i)}[l, \nu]|$ at $(l, \nu) \in \{(n_t^{(i)}, m_t^{(i)}):\ t = 1, \ldots, N_{\text{tar}}\}$ – the targets' range-Doppler bins w.r.t TX i. However, an ideal auto-correlation function is unlikely for all realizations of random c.c.s, $s^{(i)}[n, m]$, and when $\chi(l; s^{(i)}[\cdot, m]) \not\propto \delta[l]$,

(a) a large value of $|\chi(l; s^{(i)}[\cdot, m])|$ at $l \neq 0$ (i.e., sidelobe) can give rise to false-alarms and the near-far effect, similar to Remark 2; and,

11. An alternate way to greatly diminish, if not fully eliminate, the sensing interference is through CDMA (Code Division Multiple Access), where the c.c.s are spread by chirp sequences. While the low cross-correlation among chirp sequences would be effective in suppressing the sensing interference, the spreading operation is an inefficient use of bandwidth for communications. Moreover, after de-chirping, the sensing performance of CDMA signals would still depend on the auto-correlation properties of the c.c.s, as given by Remark 3.

12. The M-point Doppler DFT imposes a maximum absolute Doppler shift of $(M/2)$/CPI, where CPI is the coherent processing interval, as depicted in Fig. 2b. Any Doppler shift that falls within these limits corresponds to a unique, discrete frequency of the complex sinusoid in (6) and manifests as a peak at the appropriate Doppler bin in $R_{\text{sc}}^{(i)}[l, \nu]$. Doppler shifts outside these limits lead to Doppler/velocity ambiguity caused by aliasing of the discrete frequencies in the M-point Doppler DFT.

$$\begin{aligned} r^{(i)}[l, m] &:= \frac{1}{N} \sum_{n=-\infty}^{\infty} y^{(i)}[n, m] x^{(i)*}[n - l, m] \\ &= \underbrace{\sum_{t=1}^{N_{\text{tar}}} \alpha_t^{(i)} \chi(l - n_t^{(i)}; s^{(i)}[\cdot, m]) \exp\left(j2\pi \frac{m_t^{(i)}}{M} m\right)}_{\text{Desired signal component}} \\ &\quad + \underbrace{\sum_{q \neq i} \sum_{t'=0}^{N_{\text{tar}}} \alpha_{t'}^{(q\to i)} \varrho(l - n_{t'}^{(q\to i)}; s^{(q)}[\cdot, m], s^{(i)}[\cdot, m]) \exp\left(j2\pi \frac{m_{t'}^{(q\to i)}}{M} m\right)}_{\text{Sensing interference component}} + \tilde{w}^{(i)}[l, m], \end{aligned} \tag{9}$$

$$\text{where } \tilde{w}^{(i)}[l, m] := \frac{1}{N} \sum_{n=-\infty}^{\infty} w^{(i)}[n, m] s^{(i)*}[n - l, m]. \tag{10}$$

$$\begin{aligned} R_{\text{sc}}^{(i)}[l, \nu] &:= \sum_{m=0}^{M-1} r^{(i)}[l, m] \exp\left(-j2\pi \frac{\nu}{M} m\right) \\ &= \sum_{t=1}^{N_{\text{tar}}} \alpha_t^{(i)} \sum_{m=0}^{M-1} |\chi(l - n_t^{(i)}; s^{(i)}[\cdot, m])| \exp\left[j2\pi \left(\frac{m_t^{(i)} - \nu}{M}\right) m + \underbrace{j \arg\left(\chi(l - n_t^{(i)}; s^{(i)}[\cdot, m])\right)}_{\text{autocorr. phase noise}}\right]. \end{aligned} \tag{11}$$

(b) the phase of $\chi(l; s^{(i)}[\cdot, m])$ can impact Doppler-bin estimation, as seen in (11).

To minimize the occurrence of (a) and (b), it is desirable for $\mathbb{P}(|\chi(l; s^{(i)}[\cdot, m])| > u)$ – the tail probability of $|\chi(l; s^{(i)}[\cdot, m])|$ $(l \neq 0)$ – to decay rapidly w.r.t u. We characterize this quantity in terms of the c.c.s parameters (i.e., r_i and N) in Section III-A.

2) OFDM

The OFDM radar signal processing chain at the i-th TX involves an N-point DFT of $y^{(i)}[n, m]$ in (6) over the fast time index, n, to obtain a frequency-domain signal,[13] $Y^{(i)}[k, m]$ $(k = 0, \ldots, N-1)$, given by (12), shown at the bottom of the page. At the i-th TX, upon dividing (12) by the known $s^{(i)}[k, m]$, we obtain (14), shown at the bottom of the page,[14] where for the desired signal component, each of the terms under the summation sign is a scaled product of a pair of decoupled sinusoids – one across the subcarriers (index k), whose frequency depends on the target ranges, and another across OFDM symbols (index m), whose frequency depends on the target velocity (Doppler).[15] Hence, the target parameters can be estimated from the OFDM range-Doppler map, $R^{(i)}_{\text{OFDM}}[l, \nu]$, obtained through a combination of an N-point IDFT (over k) and an M-point DFT (over m) [36], as shown in (15), shown at the bottom of the page.

From (15), it is clear that in the absence of interference and a large enough SNR, $|R^{(i)}_{\text{OFDM}}[l, \nu]|$ would have sharp peaks only at $(l, \nu) \in \{(n_t^{(i)}, m_t^{(i)})\colon t = 1, \ldots, N_{\text{tar}}\}$ – the targets' range-Doppler bins w.r.t TX i. Furthermore, we also observe that the distortion in $R^{(i)}_{\text{OFDM}}[l, \nu]$ due to the interference from $s^{(q)}[k, m]$ is governed by the N-point IDFT of $s^{(q)}[k, m]/s^{(i)}[k, m]$ over the index k. We remark on this quantity below.

13. Although matched filtering can also be used for the OFDM waveform, the frequency domain approach of (12) is widely adopted, as it yields a higher peak-to-sidelobe ratio [36].

14. The LHS of (14) corresponds to zero-forcing equalization, for which we assume the subcarrier spacing to be larger than the inter-carrier interference caused by Doppler shifts. With minor changes, our analysis holds for other forms of equalization, as well (e.g., MMSE).

15. The OFDM cyclic prefix causes a scaling of the (discrete) Doppler frequencies in (14), but we ignore this for convenience.

$$Y^{(i)}[k,m] = \underbrace{\sum_{t=1}^{N_{\text{tar}}} \alpha_t^{(i)} s^{(i)}[k,m] \exp\left(-j2\pi \frac{n_t^{(i)}}{N} k\right) \exp\left(j2\pi \frac{m_t^{(i)}}{M} m\right)}_{\text{Desired signal returns}} + \underbrace{\sum_{q\neq i} \sum_{l=0}^{N_{\text{tar}}} \alpha_l^{(q\to i)} s^{(q)}[k,m] \exp\left(-j2\pi \frac{n_l^{(q\to i)}}{N} k\right) \exp\left(j2\pi \frac{m_l^{(q\to i)}}{M} m\right)}_{\text{Interfering signal returns}} + W^{(i)}[k,m] \tag{12}$$

$$\text{where } W^{(i)}[k,m] \coloneqq \sum_{n=0}^{N-1} w^{(i)}[n,m] \exp\left(-j2\pi \frac{k}{N} n\right). \tag{13}$$

$$\frac{Y^{(i)}[k,m]}{s^{(i)}[k,m]} = \underbrace{\sum_{t=1}^{N_{\text{tar}}} \alpha_t^{(i)} \exp\left(-j2\pi \frac{n_t^{(i)}}{N} k\right) \exp\left(j2\pi \frac{m_t^{(i)}}{M} m\right)}_{\text{Desired signal component}} + \underbrace{\sum_{q\neq i} \sum_{l=0}^{N_{\text{tar}}} \alpha_l^{(q\to i)} \frac{s^{(q)}[k,m]}{s^{(i)}[k,m]} \exp\left(-j2\pi \frac{n_l^{(q\to i)}}{N} k\right) \exp\left(j2\pi \frac{m_l^{(q\to i)}}{M} m\right)}_{\text{Sensing interference component}} + \frac{W^{(i)}[k,m]}{s^{(i)}[k,m]} \tag{14}$$

$$\begin{aligned} R^{(i)}_{\text{OFDM}}[l,\nu] &\coloneqq \frac{1}{N} \sum_{m=0}^{M-1} \sum_{k=0}^{N-1} \frac{Y^{(i)}[k,m]}{s^{(i)}[k,m]} \exp\left(j2\pi \frac{l}{N} k\right) \exp\left(-j2\pi \frac{\nu}{M} m\right) \\ &= \underbrace{\sum_{t=1}^{N_{\text{tar}}} \alpha_t^{(i)} \delta\left[l - n_t^{(i)}\right] \delta\left[\nu - m_t^{(i)}\right]}_{\text{Peaks at } (l,\nu) = \{(n_t^{(i)}, m_t^{(i)})\colon t = 1, \ldots, N_{\text{tar}}\}} \\ &\quad + \underbrace{\sum_{q\neq i} \sum_{l=0}^{N_{\text{tar}}} \alpha_l^{(q\to i)} \sum_{m=0}^{M-1} \exp\left(j2\pi \frac{(m_l^{(q\to i)} - \nu)}{M} m\right) \cdot \underbrace{\frac{1}{N} \sum_{k=0}^{N-1} \frac{s^{(q)}[k,m]}{s^{(i)}[k,m]} \exp\left(j2\pi \frac{(l - n_l^{(q\to i)})}{N} k\right)}_{\text{IDFT of } s^{(q)}[k,m]/s^{(i)}[k,m]}}_{\text{Distortion induced by sensing intf.}} \\ &\quad + \underbrace{\tilde{W}^{(i)}[l,\nu]}_{\text{Noise component}}. \end{aligned} \tag{15}$$

Definition 4: Let

$$V^{(q\to i)}[l,m] \coloneqq \frac{1}{N}\sum_{k=0}^{N-1}\frac{s^{(q)}[k,m]}{s^{(i)}[k,m]}\exp\left(j2\pi\frac{l}{N}k\right) \quad (16)$$

denote the N-point IDFT of $s^{(q)}[k,m]/s^{(i)}[k,m]$ $(q\neq i)$ over the index k.

Remark 4 (Distortion Due to Sensing Interference in the OFDM Range-Doppler Map): We may reasonably assume that for fixed m, the signals $s^{(i)}[k,m]$ and $s^{(q)}[k,m]$ are independent, as the c.c.s from different TXs are generated from mutually independent message signals. Furthermore, since $s^{(i)}[k,m]\neq 0$, it follows from Assumption 1 that $\mathbb{E}[s^{(q)}[k,m]/s^{(i)}[k,m]]=0$. Hence, $V^{(q\to i)}[l,m]$ in (16) also has zero mean, and the interference term in (15) can be viewed as a zero-mean, additive non-Gaussian distortion.

Remark 5 (Sensing Interference Management for an OFDM Waveform): Despite being zero-mean, the distortion due to the sensing interference in (15) can give rise to sidelobes in $|R^{(i)}_{\text{OFDM}}[l,\nu]|$ – accompanied by false-alarms and the near-far effect (similar to Remark 2) – if $|V^{(q\to i)}[l,m]|$ takes on a large value at a non-target range bin, l. To minimize the occurrence of these outcomes, it is desirable for $\mathbb{P}(|V^{(q\to i)}[l,m]|>u)$ – the tail probability of $|V^{(q\to i)}[l,m]|$ – to decay rapidly w.r.t u. We characterize this quantity in terms of the c.c.s parameters (i.e., r_i, r_q and N) in Section III-C.

From Remarks 2 through 5, it is clear that the sensing potential of c.c.s is intricately linked to the tail probabilities of $|\varrho(l;s^{(i)}[\cdot,m],s^{(q)}[\cdot,m])|$, $|V^{(q\to i)}[l,m]|$ and $|\chi(l;s^{(i)}[\cdot,m])|$ $(l\neq 0)$ – the first two quantities determine the sensing interference suppression capabilities of c.c.s in single-carrier and OFDM waveforms, respectively, while the third quantity impacts the sensing performance of c.c.s in a single-carrier waveform. We characterize these tail probabilities in the following section.

III. SENSING POTENTIAL OF C.C.S

Consider a pair of c.c.s blocks, $s^{(i)}[n,m]$ and $s^{(q)}[n,m]$ $(i\neq q)$, generated by message signals, $u^{(i)}[n,m]$ and $u^{(q)}[n,m]$, respectively, according to Section II-A. Since m is arbitrary, we omit this index throughout this section to simplify the notation for all the quantities of interest, such as $\chi(l;s^{(i)}[\cdot])$, $\varrho(l,s^{(i)}[\cdot],s^{(q)}[\cdot])$, $V^{(q\to i)}[l]$, etc. In deriving bounds for the tail probabilities of these quantities, we restrict our attention to their real parts; the analysis for the imaginary part follows similarly. We now introduce a few lemmas that will be used in deriving our main results later in this section.

Lemma 1 (Hoeffding's Lemma): Let X be a (real) random variable, satisfying $|X|\leq b<\infty$ with probability one, and $\mathbb{E}[X]=0$. Then, for $\lambda>0$,

$$\mathbb{E}\big[\exp(\lambda X)\big]\leq\exp\left(\lambda^2b^2/2\right). \quad (17)$$

Proof: See [37, Lemma 2.19]. ■

Lemma 2: For $\lambda\in\mathbb{R}$, and a collection of (real) identically distributed (but not necessarily independent) random variables, $X_1,\ldots,X_n$

$$\mathbb{E}\big[\exp(\lambda X_1+\cdots+\lambda X_n)\big]\leq\mathbb{E}\big[\exp(\lambda nX_1)\big]. \quad (18)$$

Proof: See Appendix II-A. ■

A. TAIL PROBABILITY OF $|\Re\{\chi(l;s[\cdot])\}|$

To further simplify the notation, we omit the index i in this subsection, and denote respectively by $\chi(l;s[\cdot])$ and $u[n]$, the auto-correlation function and the message signal associated with c.c.s, $s[n]$.

Definition 5: Let $M_l\coloneqq\lceil\frac{N-l}{K-l}\rceil$. Then, $\Re\{\chi(l;s[\cdot])\}$ can be expressed as follows :

$$\Re\{\chi(l;s[\cdot])\}\coloneqq\frac{1}{N}\left(Y_1^{(l)}+\cdots+Y_{M_l}^{(l)}\right), \quad (19)$$

where the expressions for $Y_i^{(l)}$ $(i=1,\ldots,M_l)$ are given by (20)-(21), shown at the bottom of the page. In particular, $Y_1^{(l)}\coloneqq\Re\{s[l]s^*[0]+s[l+1]s^*[1]+\cdots+s[K-1]s^*[K-1-l]\}$ denotes the sum of the first $(K-l)$ non-trivial terms in the RHS of (1), $Y_2^{(l)}$ denotes the sum of the next $(K-l)$ non-trivial terms, and so on. The last such quantity, $Y_{M_l}^{(l)}$, may contain fewer terms, but for simplicity, we assume that it contains $K-l$ non-trivial terms, as well. Decomposing $\Re\{\chi(l;s[\cdot])\}$ into partial sums in this manner, along with Assumption 2, ensures that $Y_1^{(l)}$ is a function of i.i.d random variables (i.e., the message signal $u[n]$), whose distribution can be characterized using concentration inequalities, as shown in Lemma 3 below. On the other hand, $Y_i^{(l)}$ $(i\neq 1)$, is much harder to characterize, as it is a function of a mixture of i.i.d and dependent random variables, in general. Thus, to help characterize $Y_i^{(l)}$ $(i\neq 1)$, we make the following assumption.

Assumption 4: Due to their similarity in form, we assume that $Y_1^{(l)},\ldots,Y_{M_l}^{(l)}$ are identically distributed. This is certainly true for (N,K)-linear MDS (Maximum Distance Separable) codes (e.g., the Reed-Solomon code) since any collection of K c.c.s symbols are mutually i.i.d. for such codes [38, Th. 5.4.5], and each $Y_i^{(l)}$ is a function of K c.c.s symbols, namely, $s[(i-1)(K-l)]$, $s[(i-1)(K-l)+1],\ldots,s[i(K-l)+l-1)]$. Note that $Y_1^{(l)},\ldots,Y_{M_l}^{(l)}$ are statistically dependent, in general.

$$Y_i^{(l)}\coloneqq\Re\left\{\sum_{k'=0}^{K-1-l}s[(i-1)(K-l)+k'+l]s^*[(i-1)(K-l)+k']\right\},\ (i=1,\ldots,M_l-1), \quad (20)$$

$$\text{and } Y_{M_l}^{(l)}\coloneqq\Re\big\{s\big[(M_l-1)(K-l)+l\big]s^*\big[(M_l-1)(K-l)\big]+s\big[(M_l-1)(K-l)+l+1\big]s^*\big[(M_l-1)(K-l)+1\big]$$
$$+\cdots+s[N-1]s^*[N-1-l]\big\}. \quad (21)$$

Lemma 3: For $\lambda \in \mathbb{R}$,

$$\mathbb{E}\Big[\exp\Big(\lambda Y_1^{(l)}\Big)\Big] \leq \exp\Big(\lambda^2 b^2 (K-l)/2\Big), \tag{22}$$

where b satisfies $|\Re\{s[n]s^*[n-l]\}| \leq b < \infty$, for any n, l.

Proof: See Appendix II-B. ■

Theorem 1 (Auto-correlation Upper Bound): For $u > 0$, the tail probability of $|\Re\{\chi(l; s[\cdot])\}|$ $(l \neq 0)$ satisfies the following upper bound:

$$\mathbb{P}(|\Re\{\chi(l; s[\cdot])\}| > u) \leq 2\exp(-O(rN)u^2), \tag{23}$$

as $K, N \to \infty$ and $K/N = r$.

Proof: See Appendix II-C1. ■

Remark 6 ("Extent of i.i.d-ness"): To provide intuition for the result in Theorem 1, consider $r = 1$, corresponding to an uncoded communications signal comprising i.i.d zero-mean symbols. For this special case, (23) can be interpreted as a concentration inequality closely related to the Hoeffding inequality [37, Th. 2.16], for which the order of the exponential decay is determined by the number of i.i.d random variables present (i.e., N). A c.c.s can be viewed as a mixture of i.i.d and dependent random variables/symbols; in particular, the maximal number of i.i.d symbols over a block length N equals[16] $K = rN$, which, in turn, governs the $O(rN)$ exponential decay in (23).

Theorem 2 (Auto-Correlation Lower Bound): For linear codes, the tail probability of $|\Re\{\chi(l; s[\cdot])\}|$ $(l \neq 0,\ l \ll N)$ satisfies the following lower bound for sufficiently small $u > 0$:

$$\mathbb{P}(|\Re(\chi(l; s[\cdot]))| > u) \geq \exp(-O(rN)), \tag{24}$$

where $K/N = r$.

Proof: See Appendix II-D1. ■

Remark 7 (Implication of Theorems 1 and 2): The combination of results from Theorems 1 and 2 implies that for linear codes, a faster order of decay for the auto-correlation function – in terms of the code rate and block length – is not possible. Importantly, the structure of a linear code (i.e., its generator/parity-check matrices) does not impact the order of the exponential decay.

Corollary 1 (Asymptotically Ideal Auto-Correlation): As $N \to \infty$, $|\Re\{\chi(l; s[\cdot])\}|$ converges in distribution to $\delta[l]$, i.e.,[17]

$$\lim_{N\to\infty} |\Re\{\chi(l; s[\cdot])\}| \xrightarrow{d} \delta[l]. \tag{25}$$

Proof: See Appendix II-E. ■

B. TAIL PROBABILITY OF $|\Re\{\varrho(l; s^{(i)}[\cdot], s^{(q)}[\cdot])\}|$

Assuming the symbols in $u^{(i)}[n]$ and $u^{(q)}[m]$ are mutually independent, we can derive the following bounds for $\Re\{\varrho(l; s^{(i)}[\cdot], s^{(q)}[\cdot])\}$, similar to Theorems 1 and 2.

Corollary 2 (Cross-correlation Upper Bound): For $u > 0$, the tail probability of $|\Re\{\varrho(l; s^{(i)}[\cdot], s^{(q)}[\cdot])\}|$ satisfies the following upper bound:

$$\mathbb{P}(|\Re\{\varrho(l; s^{(i)}[\cdot], s^{(q)}[\cdot])\}| > u) \leq 2\exp\Big(-O(r_{\max}N)u^2\Big), \tag{26}$$

as $K_i, K_q, N \to \infty$, $K_i/N = r_i$, $K_q/N = r_q$ and $r_{\max} \coloneqq \max(r_i, r_q)$.

Proof: See Appendix II-C2. ■

Corollary 3 (Cross-correlation Lower Bound): For linear codes, the tail probability of $|\Re\{\varrho(l; s^{(i)}[\cdot], s^{(q)}[\cdot])\}|$ satisfies the following lower bound for $l \ll N$ and sufficiently small $u > 0$:

$$\mathbb{P}(|\Re\{\varrho(l; s^{(i)}[\cdot], s^{(q)}[\cdot])\}| > u) \geq \exp(-O(r_{\text{sum}}N)), \tag{27}$$

where $K_i/N = r_i$, $K_q/N = r_q$ and $r_{\text{sum}} \coloneqq r_i + r_q$.

Proof: See Appendix II-D2. ■

Remark 8 (Implications of Corollaries 2 and 3): Similar to Remark 7, the results from Corollaries 2 and 3 imply that for linear codes, a faster order of decay for the cross-correlation function – in terms of the code rates and block length – is not possible.

Corollary 4 (Asymptotically Zero Cross-Correlation): As $N \to \infty$, $|\Re\{\varrho(l; s^{(i)}[\cdot], s^{(q)}[\cdot])\}|$ converges in distribution to 0, for any l, i.e.,

$$\lim_{N\to\infty} |\Re\{\varrho(l; s^{(i)}[\cdot], s^{(q)}[\cdot])\}| \xrightarrow{d} 0, \quad \text{any } l. \tag{28}$$

Proof: See Appendix II-E. ■

Remark 9 (Communications v/s Sensing Trade-Off w.r.t Favourable Correlation Properties): Broadly, there are two contrasting mechanisms for obtaining signals with favourable correlation properties – i.e., (near)-ideal auto-correlation function and mutually zero cross-correlation function: (a) through deterministic construction (e.g., m-sequences, Zadoff-Chu sequences etc.), or (b) through LLN, exploiting (information-bearing) randomness (e.g., c.c.s). Signals belonging to the first class typically have better correlation properties relative to c.c.s (i.e., lower sidelobes for a given N), and therefore, have excellent sensing performance, but with little communications value[18] (e.g., data rate). At the other end of the spectrum, the information-bearing randomness in c.c.s offers high communication value at the expense of potentially larger sidelobes that, in turn, may restrict its effectiveness as sensing signals to specific scenarios (e.g., small-range applications, where the near-far effect is less prevalent).

C. TAIL PROBABILITY OF $|\Re\{V^{(q\to i)}[l]\}|$

Similar to Corollaries 2 and 3, we can derive the following bounds for $\Re\{V^{(q\to i)}[l]\}$, for mutually independent $u^{(i)}[n]$ and $u^{(q)}[n]$.

16. This is true for any linear code, and does not require systematic encoding (i.e., Assumption 2).

17. Strictly speaking, the convergence is to a scaled δ-function, with the scaling factor equal to the average symbol power; see (1).

18. Some communication value can be embedded to the deterministic sensing signals by modulating them with information-bearing symbols [39], but the data rates that can be achieved by this method are very low. On the other hand, the randomness from the information-bearing symbols contributes to further reducing the sidelobe levels for such signals [40].

Corollary 5 (OFDM Interference Sidelobe Upper Bound): For $u > 0$, the tail probability of $\Re\{V^{(q\to i)}[l]\}$ $(l = 0, \ldots, N-1)$ satisfies the following upper bound:

$$\mathbb{P}\Big(|\Re\{V^{(q\to i)}[l]\}| > u\Big) \leq 2\exp\Big(-O(r_{\min}N)u^2\Big), \quad (29)$$

as $K_i, K_q, N \to \infty$, $K_i/N = r_i$, $K_q/N = r_q$, and $r_{\min} \coloneqq \min(r_i, r_q)$.

Proof: See Appendix II-C3. ■

Corollary 6: (OFDM Interference Sidelobe Lower Bound): For linear codes, the tail probability of $\Re\{V^{(q\to i)}[0]\}$ satisfies the following lower bound for sufficiently small $u > 0$:

$$\mathbb{P}(|\Re\{V^{(q\to i)}[0]\}| > u) \geq \exp(-O(r_{\text{sum}}N)), \quad (30)$$

where $K_i/N = r_i$, $K_q/N = r_q$ and $r_{\text{sum}} \coloneqq r_i + r_q$.

Proof: See Appendix II-D3. ■

Remark 10 (Implications of Corollary 5 and 6): Similar to Remarks 7 and 8, the results from Corollaries 5 and 6 imply that for linear codes, a faster order of decay for $V^{(q\to i}[l]$ – in terms of the code rates and block length – is not possible.

Corollary 7 (Asymptotic Interference Suppression): As $N \to \infty$, $|\Re\{V^{(q\to i)}[l]\}|$ converges in distribution to 0, for any l, i.e.,

$$\lim_{N\to\infty} |\Re\{V^{(q\to i)}[l]\}| \xrightarrow{d} 0, \quad \text{any } l. \quad (31)$$

Proof: See Appendix II-E. ■

Remark 11 (Single-Carrier v/s OFDM Common Waveform for ISAC – Impact of c.c.s on Sensing Performance): The similarity in the asymptotic behavior of the tail probabilities of $\chi(l; s[\cdot])$ $(l \neq 0)$, $\varrho(l; s^{(i)}[\cdot], s^{(q)}[\cdot])$ and $V^{(q\to i)}[l]$ – i.e., the $\exp(-O(rN))$ decay – implies that for any code rate, c.c.s are effective sensing signals that are robust to sensing interference for sufficiently large block lengths, with negligible difference in performance based on whether they modulate a single-carrier or OFDM waveform. We investigate this claim in the following section.

IV. SIMULATION RESULTS

In this section, we first verify the bounds derived in Section III. Next, we compare the range-Doppler sensing performance of c.c.s in interference-limited operation with that of a benchmark interference-free FMCW waveform. We then conclude this section by investigating the impact of interleaving in Fig. 3.

A. PEAK-TO-SIDELOBE RATIO AND SENSING INTERFERENCE SUPPRESSION OF C.C.S

The sidelobes[19] of $\chi(l; s[\cdot])$, can be measured using the *peak-to-sidelobe ratio* (PSLR) metric, defined as follows:

$$\text{PSLR (dB)} \coloneqq -20\log_{10}\big(\max_{l\neq 0} |\chi(l; s[\cdot])|\big), \quad (32)$$

where a large positive value signifies a closer approximation to $\delta[l]$. Similarly, replacing $\chi(l; s[\cdot])$ with $\varrho(l; s^{(i)}[\cdot], s^{(q)}[\cdot])$ and $V^{(q\to i)}[l]$ in (32) yields a metric that measures the extent of interference suppression provided by c.c.s for single-carrier and OFDM waveforms, respectively.

Figs. 4a and 4b respectively plot the median PSLR and interference suppression (obtained over 10000 simulation instances) as a function of N, for LDPC and Polar coded signals[20] at two rates – 120/1024 and 682.5/1024 – corresponding to the smallest code rates for which QPSK and 256QAM modulation are used in 5G NR, respectively [41, Table 5.1.3.1-2]. We make the following remarks, based on the plotted curves:

Remark 12 (3dB Increase in (Median) PSLR and Interference Suppression With a Doubling of the Block Length): Theorem 1, Corollary 2 and Corollary 5 each provide a lower bound for (32),[21] which suggests that the median PSLR and interference suppression provided by c.c.s should eventually increase by at least 3dB when the block length is doubled; for the values of N considered, we observe that this holds true, as the curves corresponding to c.c.s are nearly parallel to those obtained from the bounds.

Remark 13 (Impact of Code structure): The convergence behaviour of $\chi(l; s[\cdot])$ $(l \neq 0)$, $\varrho(l; s^{(i)}[\cdot], s^{(q)}[\cdot])$ and $V^{(q\to i)}[l]$ is governed by LLN and the "extent of i.i.d-ness" among the codeword symbols (Remark 6), which does not depend on the code structure (i.e., Polar or LDPC) for fixed r, N and modulation scheme. Hence, the code structure has negligible impact on the median PSLR and interference suppression provided by c.c.s.

Remark 14 (Effective Sensing Interference Suppression): Higher interference suppression at larger block lengths is a noteworthy feature of c.c.s that is shared with other well-known deterministic sensing signals (e.g., m-sequences), but is not a universal feature among sensing signals, in general; for instance, a pair of FMCW chirp signals with different chirp slopes gives rise to a distinctive interference pattern that is not straightforward to eliminate [42], [43]. However, we note that this robustness is restricted to multi-user interference, and not any form of adversarial interference, like jamming.

Remark 15 (Near-Far Effect): The PSLR of a sensing waveform is a measure of its robustness to the near-far effect. To illustrate this, consider two identical targets – one near and one far from the radar – and suppose $N = 1024$, for which the median PSLR is ≈ 25dB. Due to R^{-4} attenuation, the radar return from the far target is > 25dB weaker than that of the near one, when the former's range exceeds the

19. The sidelobes of $\chi(l; s[\cdot])$ have two main contributors: (a) the correlation properties of $s[n]$, and (b) timing errors. These two factors are independent, in the sense that even if $\chi(l; s[\cdot]) = \delta[l]$, sidelobes can still be present if there is a timing offset. In this paper, we focus on the sidelobes due to (a) only, assuming no timing errors. The sidelobes due to (b) can be minimized using a pulse shape with a fast roll-off (e.g., root-raised cosine or Gaussian pulses).

20. Unlike the analysis in Section III, we have not imposed systematic encoding (Assumption 2) in our simulations.

21. A lower bound is obtained for a suitable scaling factor of the $O(rN)$ term. We have assumed a value of $1/2b^2$, where b is defined in Lemma 3 and depends on the symbol constellation.

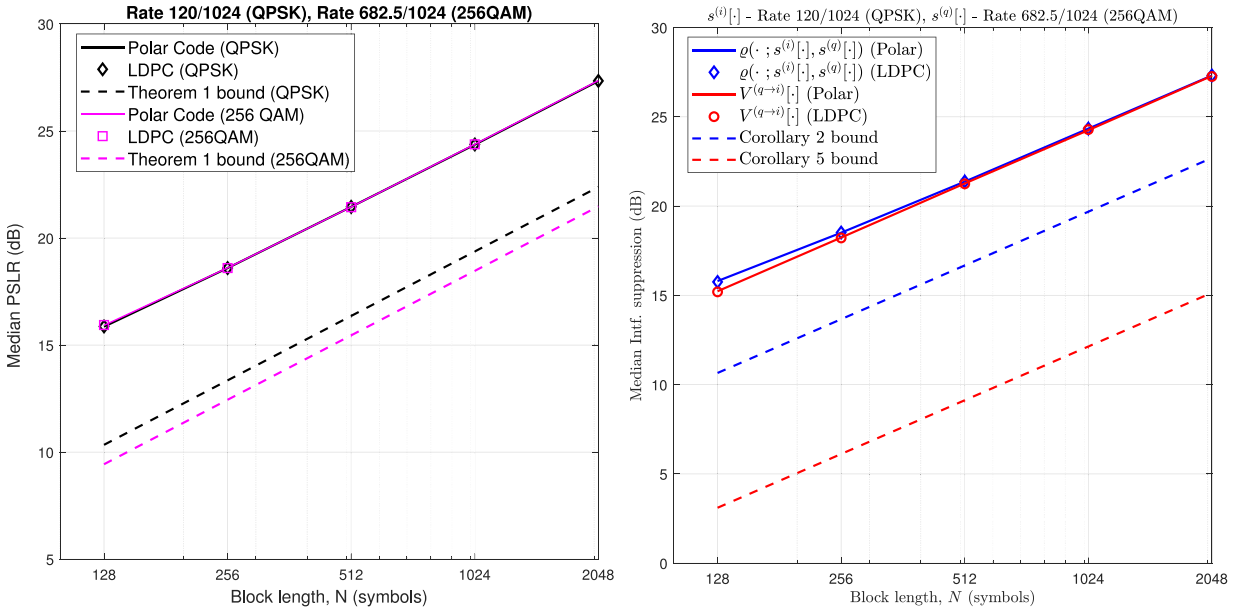

(a) PSLR of c.c.s

(b) Interference Suppression of c.c.s

FIGURE 4. The median PSLR and mutual interference suppression provided by c.c.s increases by approximately 3dB when the block length is doubled, mirroring the bounds in Theorem 1, Corollary 2 and Corollary 5.

TABLE 1. List of simulation parameters for the near-far target scenario in Section IV-B.

Bandwidth, B	1 GHz	Target Ranges (d_1, d_2)	2m, 4m
Range resolution, Δr	0.15m	Target Range bins $(n_1^{(1)}, n_2^{(1)})$	14, 27
Block length, N	1024 (symbols)	Target speeds (v_1, v_2)	10mph, 15mph
Largest range bin, $n_{\max}$	32	Target Doppler bins $(m_1^{(1)}, m_2^{(1)})$	516, 518
Maximum detectable range	4.65m	Target return gains $(\alpha_1^{(1)}, \alpha_2^{(1)})$	1, $10^{-12/10}$
Carrier frequency, f_c	140 GHz	Intf. range (d_{intf})	4.3m
No. of blocks, M	1024	Intf. range bin $(n_0^{(2\to1)})$	29
Velocity resolution, Δv	2.28mph	Intf. speed (v_{intf})	15mph
Coding	Polar Code $(r = 120/1024)$	Intf. Doppler bin $(m_0^{(2\to1)})$	518
Modulation	QPSK	Intf. gain $(\alpha_0^{(2\to1)})$	$\sqrt{10^{11/10}}$
SNR (w.r.t near target)	0dB		
SIR (w.r.t near target)	-11dB		

latter's by a factor > 4.2. Thus, c.c.s are effective sensing signals only up to a certain maximum range that depends on the block length. We explore this in more detail in Section IV-B.

B. SENSING PERFORMANCE OF C.C.S AND THE NEAR-FAR EFFECT

In this subsection, we explore the sensing performance of c.c.s in an interference-limited scenario featuring the near-far effect, by considering the radar scene in Fig. 1b with TX 1 as the desired radar, TX 2 as the interfering radar, and two (point) targets (i.e., $M_r = N_{\text{tar}} = 2$). We model this scene in terms of the notation in Section II-B below (see Table 1 for a full list of simulation parameters):

(i) With respect to TX 1, suppose the near target is at $d_1 = 2$m and moving at $v_1 = 10$mph, while the far target is at $d_2 = 4$m and moving at $v_2 = 15$mph in the same direction as the near target. Assuming a signal bandwidth of 1 GHz, a carrier frequency of 140 GHz, and $M = N = 1024$, the targets' (range, Doppler) bins are $(n_1^{(1)}, m_1^{(1)}) = (14, 516)$ and $(n_2^{(1)}, m_2^{(1)}) = (27, 518)$. Note that the Doppler bins can vary for a different choice of M.

(ii) We assume that the sensing interference experienced at TX 1 is dominated by the signal received along the direct path, TX 2 $\to$ TX 1, corresponding to $l = 0$ in the RHS of (7). Hence, for simplicity, we consider only this component and assume $(n_0^{(2\to1)}, m_0^{(2\to1)}) = (29, 518)$, which corresponds to TX 2 situated at $d_{\text{intf}} = 4.3$m away from TX 1 and moving at $v_{\text{intf}} = 15$mph – i.e., close to and moving as fast as the far target in (i) above.

(iii) For the amplitudes of the desired radar returns, we assume $\alpha_1^{(1)} = 1$ and $\alpha_2^{(1)} = 10^{-12/10}$, resulting in a 24dB difference between the return energy from the

near and far targets. Of this, 12dB is due to R^{-4} attenuation [i.e., $\propto (d_1/d_2)^4$], while the rest is accounted for by assuming a weaker radar cross section for the far target.

(iv) Unlike the radar returns, the interference signal experiences R^{-2} attenuation, and therefore, $\frac{|\alpha_0^{(2\to 1)}|^2}{|\alpha_1|^2} \propto \frac{d_1^4}{d_{\text{intf}}^2}$, based on a unit radar cross section for the near target. Hence, we assume $\alpha_0^{(2\to 1)} = \sqrt{10^{11/10}}$, resulting in an SIR of -11dB w.r.t the near target. With these parameter values, a couple of key question are whether (a) the strong signal from the *interference bin* is suppressed, and (b) the weak return from the far target bin is visible in the range-Doppler maps? We explore these in Fig. 5.

(iv) The c.c.s blocks, $s^{(1)}[n, m]$ and $s^{(2)}[n, m]$ – transmitted by TX 1 and TX 2, respectively – are obtained from a rate 120/1024 Polar code, followed by QPSK modulation. The corresponding message blocks, $u^{(1)}[n, m]$ and $u^{(2)}[n, m]$, are mutually independent. Finally, the SNR w.r.t to the near target is 0dB.

The presence/absence of a target in (range, Doppler) bin (l, ν) is decided using a threshold rule, as follows:

$$H_1(H_0)\text{: Target present (absent)}$$
$$|R_w^{(1)}[l, \nu]| \underset{H_0}{\overset{H_1}{\gtrless}} \eta, \quad w \in \{\text{sc, OFDM}\}. \tag{33}$$

where $R_w^{(1)}[l, \nu]$ denotes the range-Doppler map at TX 1 for $w \in \{\text{sc, OFDM}\}$, defined in (11) and (15). For a given threshold, η, the sensing performance of c.c.s is characterized by the detection and false alarm probabilities – denoted by $P_d^w(\eta)$ and $P_f^w(\eta)$, respectively – and defined in (34)–(35), shown at the bottom of the page:

Fig. 5 shows the range-Doppler maps for a given realization of c.c.s and FMCW waveforms. We observe that:

- For $N = 1024$, the median PSLR [$\approx$ 25dB in Fig. 4(a)] is nearly at par with the difference in return strengths between the near and far targets. Despite this, the far target is clearly "visible" because the targets are situated in different Doppler bins, which provides nearly 30dB of additional sidelobe suppression for $M = 1024$ through the Doppler DFT.
- For $N = 1024$, the nearly 25dB median interference suppression in Fig. 4b seems insufficient, at first glance, to detect the weaker target in the face of strong interference from a nearby bin. However, from (32), we see that the interference suppression is defined in terms of the maximum sidelobe level *across all* bins, which can be a conservative estimate of the sidelobe levels at a specific interference bin. In this case, we see that the strong interference signal from a nearby bin is adequately suppressed and the weaker target is clearly visible. However, the essence of Remark 15 – i.e., a limit on the maximum target range imposed by the sidelobes of c.c.s – remains valid.
- The magnitude of the c.c.s range-Doppler maps at the target bin locations is nearly the same as that for the FMCW waveform – both with and without interference and for both single-carrier and OFDM waveforms. This is consistent with the results from Section III that c.c.s yield asymptotically ideal range-Doppler maps (i.e., δ-function spikes at the target bins) at large block lengths, despite the presence of sensing interference.
- The large sidelobes across the range bins in the FMCW range-Doppler map are a consequence of rectangular windowing assumed for the range FFT. Lower sidelobe levels can be achieved through a better choice of windowing function, which we do not pursue as it is beyond the scope of this paper.

Fig. 6 compares the detection performance of c.c.s, where we observe the following:

- For a threshold-based detection rule of the form given by (33), the detection probability exhibits a step-like behavior with increasing η, where for small η, both targets are detected; followed by a regime where only the near target is detected; before none of the targets is detected.
- For a small set of thresholds, the FMCW waveform has a higher false-alarm probability than c.c.s without interference (see inset), due to the large sidelobes induced by rectangular windowing, as discussed w.r.t Fig. 5. Thus, window functions that result in lower sidelobes would also cause the false-alarm probability curve in Fig. 6 to shift leftward.
- Despite strong interference (-11dB SIR), the detection performance of c.c.s matches that of an interference-free FMCW waveform, and is only marginally worse – in terms of the behavior of the false-alarm probability – than c.c.s without interference.
- The *sweet-spot* threshold(s) for a given waveform are those that result in both targets being detected, without

$$P_d^w(\eta) := \underbrace{\mathbb{P}\Big(\Big|R_w^{(1)}[n_1^{(1)}, m_1^{(1)}]\Big| > \eta; \Big|R_w^{(1)}[n_2^{(1)}, m_2^{(1)}]\Big| > \eta\Big)}_{\text{Both targets detected}}$$
$$+ \underbrace{\frac{1}{2}\mathbb{P}\Big(\Big|R_w^{(1)}[n_1^{(1)}, m_1^{(1)}]\Big| > \eta; \Big|R_w^{(1)}[n_2^{(1)}, m_2^{(1)}]\Big| \le \eta\Big)}_{\text{Only near target detected (hence, the 1/2 scaling factor)}} + \underbrace{\frac{1}{2}\mathbb{P}\Big(\Big|R_w^{(1)}[n_1^{(1)}, m_1^{(1)}]\Big| \le \eta; \Big|R_w^{(1)}[n_2^{(1)}, m_2^{(1)}]\Big| > \eta\Big)}_{\text{Only far target detected (hence, the 1/2 scaling factor)}}, \tag{34}$$

$$P_f^w(\eta) := \mathbb{P}\Big(\Big|R_w^{(1)}(l, \nu)\Big| > \eta, \text{ where } (l, \nu) \notin \{(n_1^{(1)}, m_1^{(1)}), (n_2^{(1)}, m_2^{(1)})\}\Big). \tag{35}$$

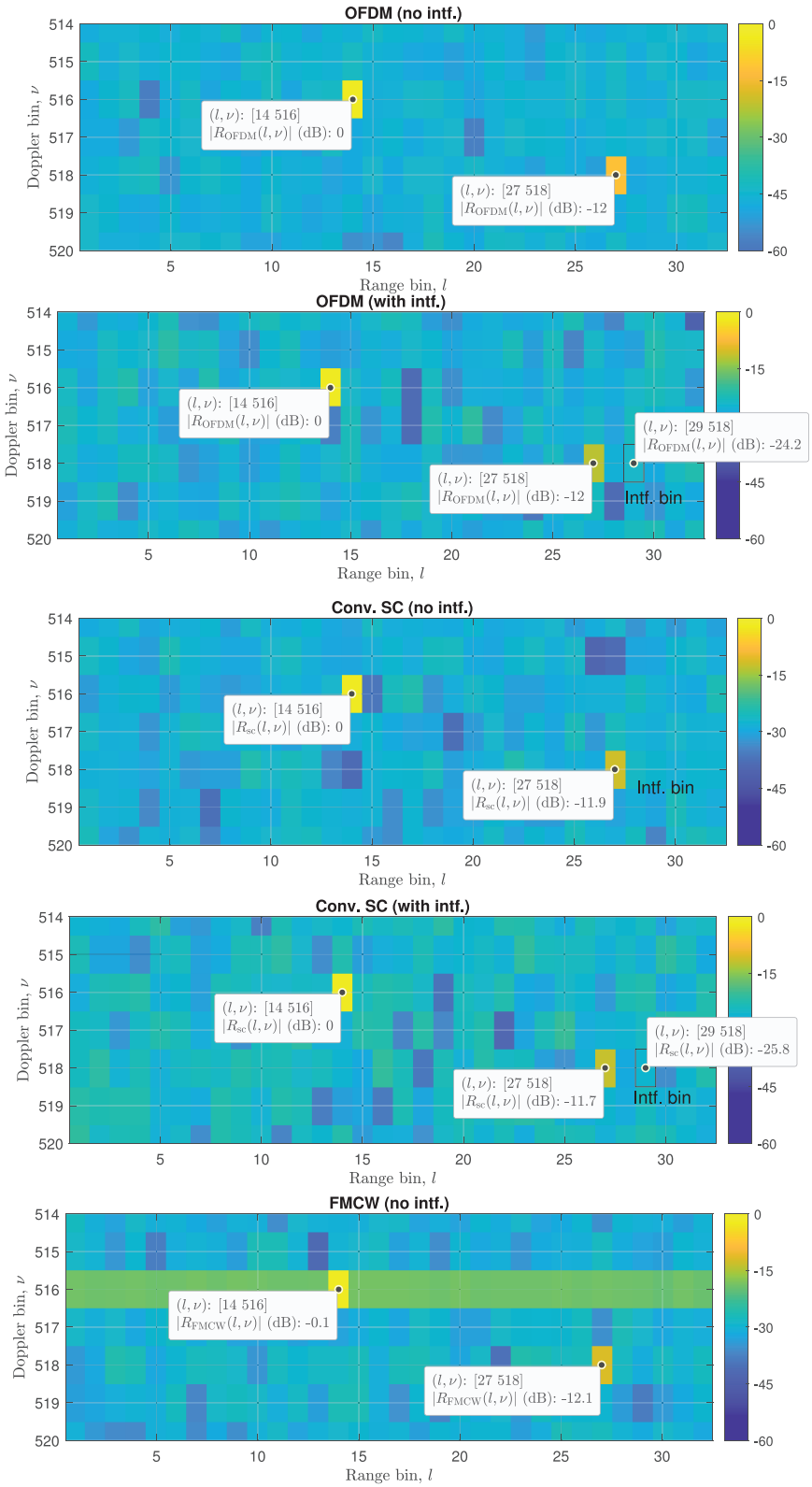

FIGURE 5. For the simulation setup in Table 1, the magnitude of the range-Doppler maps at the target bin locations – (14, 516) and (27, 518) – are similar for both FMCW and c.c.s waveforms, even at −11dB SIR for the latter.

any false-alarms. From the previous bullet point, it follows that the sweet spot regions for c.c.s and FMCW mostly coincide.

C. THE ROLE OF INTERLEAVING

A key component of the BICM model for c.c.s in Fig. 3 is the interleaver, whose role is to produce mutually uncorrelated

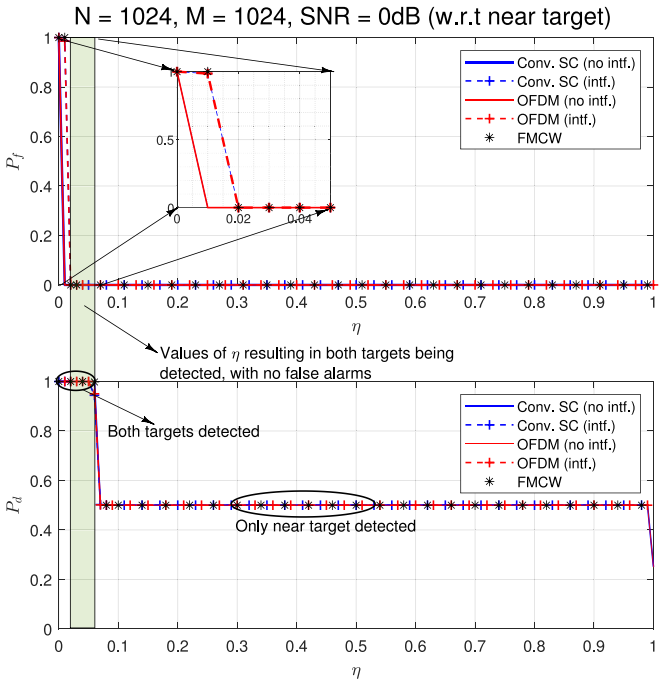

FIGURE 6. Due to the similarity of the range-Doppler maps in Fig. 5, the curves corresponding to the detection and false-alarm probabilities for all the waveforms also exhibit considerable overlap.

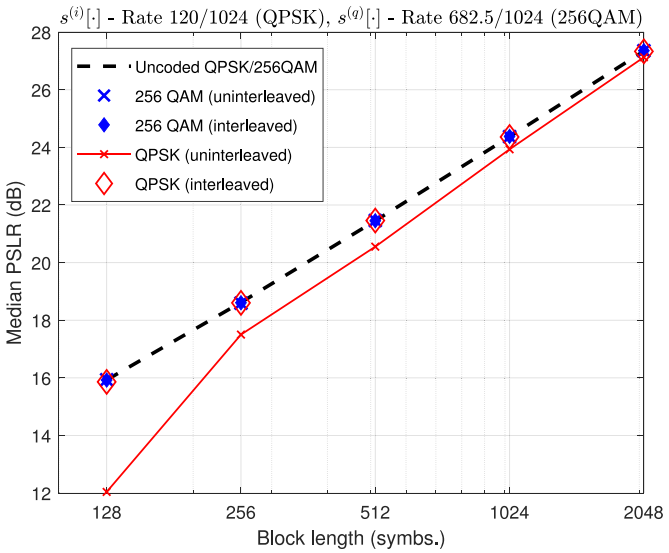

FIGURE 7. Interleaving improves the PSLR of c.c.s, especially for small code rates and block lengths.

c.c.s symbols (Assumption 3) by subjecting the codeword bits to a uniformly distributed random permutation. To see the effect of interleaving, Fig. 7 compares the median PSLR (and by extension, interference suppression) for Polar coded c.c.s with and without interleaving. We make the following observations:

- From the bound in Theorem 1, we observe that the median PSLR (in dB) is proportional to $10\log_{10}(rN)$. Hence, for code rates *sufficiently close* to one, the block length has a much greater influence on the median PSLR. This is reflected in the curves for uninterleaved c.c.s, where (a) the median PSLR increases with r for fixed N, but the performance at $r = 682.5/1024$ practically coincides with that of an uncoded signal (i.e., $r = 1$); and (b) the difference in the median PSLR between low and high rate c.c.s diminishes with increasing N.
- Regardless of the modulation and coding scheme, the BICM c.c.s has the same median PSLR as that of an uncoded signal. This suggests that the BICM c.c.s is *ergodic*, despite exhibiting statistical dependence over a block. The seeming ergodicity of the BICM c.c.s may also explain why the bounds derived in Section III are conservative in Fig. 4 – the bounds are based on the extent of i.i.d-ness within c.c.s (see Remark 6) and not on their ergodic properties.

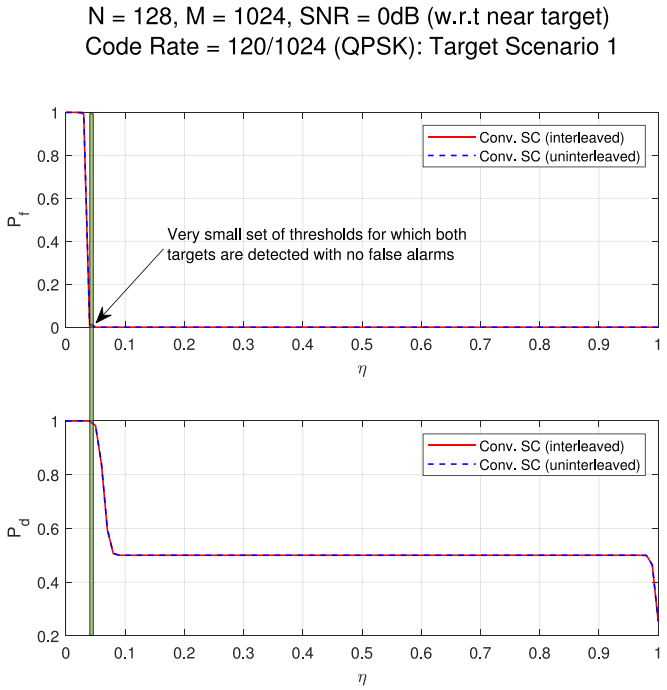

FIGURE 8. Near-far target scenario from Table 1, but with $N = 128$. A median PSLR of at most 16dB for $N = 128$ from Fig. 7 means that the far target return is buried by the near target and interference sidelobes, regardless of interleaving.

In essence, the most noticeable improvement in median PSLR due to interleaving occurs at *small code rates and block lengths*. However, in this regime, differences in other metrics like the detection and false-alarm probabilities depend on the target scenario.[22] To explore this notion, we first consider the same target setup from Section IV-B, for which Fig. 8 plots the detection and false-alarm probability curves[23] for BICM and uninterleaved c.c.s for $N = 128$. We

22. The PSLR is attractive precisely because it allows an evaluation of sensing performance that is independent of the target scenario.

23. In Figs. 8 and 9, we have omitted the curves for the OFDM waveform to avoid cluttering the figure, as they coincide with the single-carrier curves.

observe that there is negligible difference in performance associated with interleaving, which might seem counterintuitive at first to Fig. 7. However, the far target return is 24dB weaker than the near target, whereas the median PSLR for $N = 128$ is no more than 16dB (see Fig. 7). Thus, regardless of interleaving, it is highly likely that the far target is buried by the auto-correlation sidelobes from the near target and the interference (cross-correlation) sidelobes. This is evidenced by the fact that there is practically no value of the threshold, η, in Fig. 8 that results in both targets being detected with no false-alarms.

Motivated by the PSLR values in Fig. 7, we consider an alternate target scenario, which is identical to Table 1, except for the amplitude of the radar returns. Specifically, we assume the far target return to be 14dB weaker than the near target (i.e., $\alpha_2^{(1)} = \sqrt{10^{-14/10}}$), and the interference return has the same strength as the near target return (i.e., $\alpha_0^{(2\to1)} = \alpha_1^{(1)} = 1$). For this scenario, Fig. 9 plots the false-alarm and detection probability curves. We observe that in the absence of interleaving, there is a marginal loss in performance in the form of higher false-alarm probabilities for a given η. However, this loss is performance is only noticeable at certain η.

To summarize, the interleaver is effective in *guaranteeing* mutually uncorrelated c.c.s symbols, regardless of the code rate and coding scheme. Thus, if the encoder in Fig. 3 generates mutually uncorrelated codeword bits, then there is no additional benefit to interleaving from a sensing perspective. Otherwise, in the absence of interleaving, any deterioration in PSLR – and by extension, sensing performance – depends on the codeword statistics and the target scenario (extent of the near-far effect).

We conclude this section by noting that the results from Figs. 4 through 6 corroborate the bounds derived in Section III, thereby demonstrating that c.c.s are effective sensing signals even in the presence of strong sensing interference, with negligible difference in performance based on whether they modulate a single-carrier or OFDM waveform.

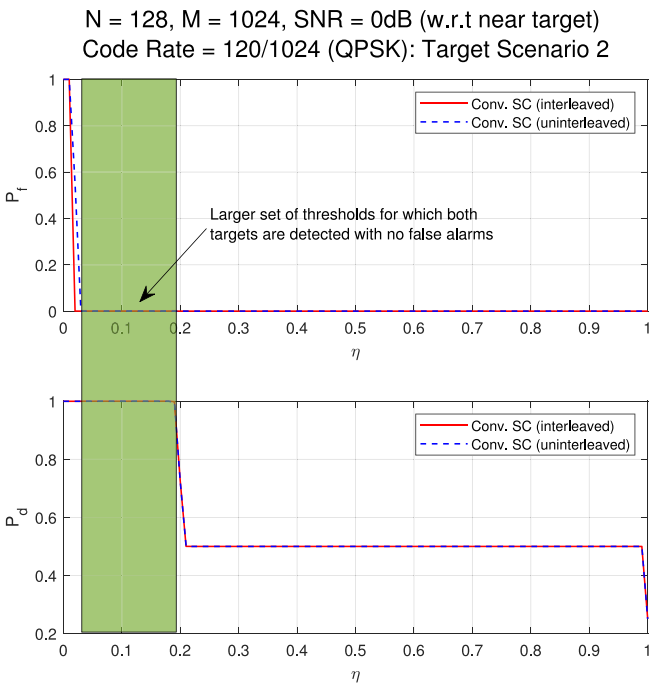

FIGURE 9. Modified near-far target scenario: Far target return 14dB weaker than near target return, interference return 0dB stronger than near target return. Firstly, as opposed to Fig. 8, there are a range of η for which both targets are detected without false alarms, regardless of interleaving. Moreover, in the absence of interleaving, there is a marginal loss in performance (i.e., higher false-alarm probability for a given η). However, this loss is performance is only noticeable at certain η.

V. CONCLUDING REMARKS

In this paper, we explored the sensing potential of c.c.s in interference-limited ISAC scenarios featuring both multi-user communications and sensing interference, with the latter dominating the former. We started by identifying – based on whether the waveform was single-carrier or OFDM – functions of c.c.s that could adversely affect its sensing performance through large sidelobes. We then derived upper bounds for the tail probabilities of the sidelobe levels that decayed exponentially in terms of the code rate-block length product. These bounds suggested that c.c.s were effective sensing signals that were robust to sensing interference at sufficiently large block lengths for any fixed code rate, with negligible difference in performance based on whether they modulate a single-carrier or OFDM waveform. The latter implication was verified through simulations, where we observed that the sensing performance of c.c.s – in terms of detection and false-alarm probabilities – was at par with that of the interference-free FMCW waveform for both single-carrier and OFDM waveforms, even at an SIR of -11 dB. Thus, our results imply that (a) a common ISAC waveform (either single- or multi-carrier, but) largely comprising coded data symbols is an effective sensing signal at large block lengths, and (b) in multi-user ISAC scenarios with such a waveform, sensing interference management essentially *takes care of itself* for monostatic radars, and is relatively simpler than communications interference management. These are highly favourable results for the evolution of existing wireless networks to support sensing applications while also maximizing the communications spectral efficiency, as the sensing functionality does not impose additional constraints on the available resources, either in the form of needing more reference signals or orthogonal resource allocation across users.

APPENDIX I
REPETITION CODES: INTERLEAVING MITIGATES CORRELATION ACROSS CODEWORD BITS

Let $\mathbf{c} = [c_0 \ \cdots \ c_{\gamma K-1}] = [\underbrace{b_0 \ \cdots \ b_{K-1} \ \cdots \ b_0 \ \cdots \ b_{K-1}}_{\gamma \, times}]$ denote the codeword corresponding to the i.i.d. Bernoulli$(1/2)$ message vector $\mathbf{b} = [b_0 \ \cdots b_{K-1}]$ for a rate $1/\gamma$ repetition code, where $\gamma \in \{1, 2, \ldots, \}$. Then,

for $i \neq j$ and $j > i$, the correlation coefficient of c_i and c_j – denoted by $\rho(c_i, c_j)$ – is given by:

$$\rho(c_i, c_j) = \begin{cases} 1, & |j-i| \mod K = 0 \\ 0, & \text{else}, \end{cases} \tag{36}$$

which captures the fact that codeword bits that are separated by a multiple of K are fully correlated.

Let $\tilde{\mathbf{c}} = \pi(\mathbf{c})$ denote the interleaved codeword, where $\pi(.)$ is a permutation of bit locations such that: (a) $\pi(i) = i$, for $i = 0, \ldots, K-1$ (i.e., systematic encoding from Assumption 2), and (b) $[\pi(K), \cdots, \pi(\gamma K - 1)]$ is a uniformly distributed random permutation of $\{K, K+1, \ldots, \gamma K - 1\}$. Then, for $i \neq j$ and $j > i$

$$\begin{aligned} \rho(\tilde{c}_i, \tilde{c}_j) &= \mathbb{P}(|\pi^{-1}(i) - \pi^{-1}(j)| \mod K = 0) \\ &= \begin{cases} 0, & i,j \in \{0, \ldots, K-1\} \\ \frac{\gamma-1}{(\gamma-1)K}, & i \in \{0, \ldots, K-1\}, \\ & j \in \{K, \ldots, \gamma K - 1\} \\ \frac{\gamma-2}{(\gamma-1)K-1}, & i,j \in \{K, \ldots, \gamma K - 1\}. \end{cases} \end{aligned} \tag{37}$$

From (37), we see that $\rho(\tilde{c}_i \tilde{c}_j) \to 0$ as $K \to \infty$. Thus, the interleaved codeword bits are asymptotically uncorrelated.

APPENDIX II
PROOFS

A. PROOF OF LEMMA 2

From the AM-GM inequality, we have for $\lambda \in \mathbb{R}$,

$$\exp(\lambda X_1 + \cdots + \lambda X_n) \leq \frac{1}{n} \sum_{i=1}^{n} \exp(\lambda n X_i) \tag{38}$$

Applying the $\mathbb{E}[\cdot]$ operator to both sides of the above inequality, we obtain

$$\mathbb{E}\big[\exp(\lambda X_1 + \cdots + \lambda X_n)\big] \leq \mathbb{E}\big[\exp(\lambda n X_1)\big] \tag{39}$$

B. PROOF OF LEMMA 3

Let $\mathbf{u}^{(K-2)} := [u[0], \ldots, u[K-2]]$. From Assumption 2 and (20), we have

$$\begin{aligned} Y_1^{(l)} &= \Re\big\{u[l]u^*[0] + u[l+1]u^*[1] + \cdots \\ &\quad + u[K-1]u^*[K-1-l]\big\} \\ &= A(\mathbf{u}^{(K-2)}) + B(u[K-1]), \end{aligned} \tag{40}$$

$$\begin{aligned} \text{where } A(\mathbf{u}^{(K-2)}) &:= \Re\big\{u[l]u^*[0] + u[l+1]u^*[1] + \cdots \\ &\quad + u[K-2]u^*[K-2-l]\big\}, \end{aligned} \tag{41}$$

$$\text{and } B(u[K-1]) := \Re\big\{u[K-1]u^*[K-1-l]\big\}. \tag{42}$$

Conditioning on $\mathbf{u}^{(K-2)}$, $\mathbb{E}[\exp(\lambda Y_1^{(l)})]$ can be written as:

$$\begin{aligned} &\mathbb{E}\Big[\exp\Big(\lambda Y_1^{(l)}\Big)\Big] \\ &= \mathbb{E}\Big[\mathbb{E}\Big[\exp\Big(\lambda Y_1^{(l)}\Big)|\mathbf{u}^{(K-2)}\Big]\Big] \\ &= \mathbb{E}\Big[\exp\Big(\lambda A(\mathbf{u}^{(K-2)})\Big)\mathbb{E}\Big[\exp(\lambda B(u[K-1]))|\mathbf{u}^{(K-2)}\Big]\Big], \end{aligned} \tag{43}$$

where the inner conditional expectation in (43) is w.r.t $u[K-1]$. Since $u[K-1]$ is independent of $\mathbf{u}^{(K-2)}$, we have

$$\begin{aligned} &\mathbb{E}\Big[\exp(\lambda B(u[K-1]))|\mathbf{u}^{(K-2)}\Big] \\ &= \mathbb{E}\big[\exp(\lambda B(u[K-1]))\big] \\ &\leq \exp\left(\frac{\lambda^2 b^2}{2}\right), \end{aligned} \tag{44}$$

where the latter inequality stems from Lemma 1, as $|\Re\{u[K-1]u^*[K-1-l]\}| = |\Re\{s[K-1]s^*[K-1-l]\}| \leq b$. Thus, from (43) and (44),

$$\mathbb{E}\Big[\exp\Big(\lambda Y_1^{(l)}\Big)\Big] \leq \exp\left(\frac{\lambda^2 b^2}{2}\right)\mathbb{E}\Big[\exp\Big(\lambda A\Big(\mathbf{u}^{(K-2)}\Big)\Big)\Big]. \tag{45}$$

Repeating the above steps recursively by conditioning on $\mathbf{u}^{(K-3)}, \mathbf{u}^{(K-4)}$ and so on, we get,

$$\mathbb{E}\Big[\exp\Big(\lambda Y_1^{(l)}\Big)\Big] \leq \exp\left(\frac{\lambda^2 b^2}{2}(K-l)\right)$$

C. PROOFS OF THEOREM 1, COROLLARY 2 AND COROLLARY 5

1) THEOREM 1

We use the Chernoff bound to prove our result. For $u > 0$,

$$\begin{aligned} &\mathbb{P}(\Re\{\chi(l; s[\cdot])\} > u) \\ &\overset{(a)}{=} \mathbb{P}\Big(Y_1^{(l)} + \cdots + Y_{M_l}^{(l)} > Nu\Big) \\ &= \mathbb{P}\Big(\exp\Big[\lambda Y_1^{(l)} + \cdots + \lambda Y_{M_l}^{(l)}\Big] > \exp(\lambda N u)\Big) \ (\lambda > 0) \\ &\overset{(b)}{\leq} \exp(-\lambda N u)\ \mathbb{E}\Big[\exp\Big(\lambda Y_1^{(l)} + \cdots + \lambda Y_{M_l}^{(l)}\Big)\Big] \qquad (46) \\ &\overset{(c)}{\leq} \exp(-\lambda N u)\ \mathbb{E}\Big[\exp\Big(\lambda M_l Y_1^{(l)}\Big)\Big] \qquad (47) \\ &\overset{(d)}{\leq} \exp\left(-\lambda N u + \frac{\lambda^2 M_l^2 b^2}{2}(K-l)\right). \qquad (48) \end{aligned}$$

where (a), (b), (c) and (d) above arise from Definition 5, the Markov inequality, Lemma 2 and Lemma 3, respectively. The tightest upper bound in (48) is obtained at $\lambda = Nu/(b^2 M_l^2 (K-l))$, by equating the derivative of the argument of the exponent to zero. Substituting this value in (48), we obtain

$$\mathbb{P}(\Re\{\chi(l; s[\cdot])\} > u) \leq \exp\left(-\frac{N^2 u^2}{2b^2 M_l^2 (K-l)}\right). \tag{49}$$

Similarly,

$$\begin{aligned} &\mathbb{P}(\Re\{\chi(l; s[\cdot])\} < -u) \\ &= \mathbb{P}(Y_1^{(l)} + \cdots + Y_{M_l}^{(l)} < -Nu) \\ &= \mathbb{P}\Big(\exp(\lambda Y_1^{(l)} + \cdots + Y_{M_l}^{(l)}) > \exp(-\lambda N u)\Big) \ (\lambda < 0). \end{aligned} \tag{50}$$

The rest of the analysis follows along the same lines as (46)-(48), with $\lambda = -Nu/(b^2 M_l^2 (N-l))$, resulting in the following bound

$$\mathbb{P}(\Re\{\chi(l; s[\cdot])\} < -u) \leq \exp\left(-\frac{N^2 u^2}{2b^2 M_l^2 (K-l)}\right). \tag{51}$$

$$\tilde{Y}_a^{(l)} \coloneqq \Re\left\{\sum_{k'=0}^{\tilde{K}-1} s^{(i)}[(a-1)\tilde{K}+l+k']s^{(q)*}[(a-1)\tilde{K}+k']\right\},\ a=1,\ldots,\tilde{M}_l-1 \tag{54}$$

$$\tilde{Y}_{\tilde{M}_l}^{(l)} \coloneqq \Re\Big\{s^{(i)}\Big[\Big(\tilde{M}_l-1\Big)\tilde{K}+l\Big]s^{(q)*}\Big[\Big(\tilde{M}_l-1\Big)\tilde{K}\Big]+s^{(i)}\Big[\Big(\tilde{M}_l-1\Big)\tilde{K}+l+1\Big]s^{(q)*}\Big[\Big(\tilde{M}_l-1\Big)\tilde{K}+1\Big] + \cdots + s^{(i)}[N-1]s^{(q)*}[N-1-l]\Big\} \tag{55}$$

Combining (49) and (51), we get

$$\mathbb{P}(|\Re\{\chi(l;s[\cdot])\}|>u) \le 2\exp\left(-\frac{N^2u^2}{2b^2M_l^2(K-l)}\right). \tag{52}$$

As $K, N \to \infty$ with $K/N = r$, $N^2/(2b^2M_l^2(K-l)) = O(rN)$. This completes the proof.

2) COROLLARY 2

Let $\tilde{K} \coloneqq \max(K_i - l, K_q)$. Similar to Definition 5, $\Re\{\varrho(l; s^{(i)}[\cdot], s^{(q)}[\cdot])\}$ can be expressed as follows:

$$\Re\{\varrho(l;s^{(i)}[\cdot],s^{(q)}[\cdot])\} \coloneqq \tfrac{1}{N}\Big(\tilde{Y}_1^{(l)}+\cdots+\tilde{Y}_{\tilde{M}_l}^{(l)}\Big), \tag{53}$$

where $\tilde{M}_l \coloneqq \lceil \frac{N-l}{\tilde{K}} \rceil$, and $\tilde{Y}_a^{(l)}$ $(a = 1, \ldots, \tilde{M}_l)$ are given by (54)-(55), shown at the bottom of the page. The remainder of the proof follows along the same lines as Appendix II-C1.

3) COROLLARY 5

Let $K_0 \coloneqq \min(K_i, K_q)$. Similar to Definition 5, $\Re\{V^{(q\to i)}[l]\}$ can be expressed as follows :

$$\Re\{V^{(q\to i)}[l]\} \coloneqq \frac{1}{N}\big(T_1[l]+\cdots+T_{M_0}[l]\big),$$

$$\text{where } M_0 \coloneqq \left\lceil \frac{N}{K_0} \right\rceil,$$

$$T_i[l] \coloneqq \Re\left\{\sum_{k=(i-1)K_0}^{iK_0-1} \frac{s^{(q)}[k]}{s^{(i)}[k]}\exp\left(j2\pi\frac{l}{N}k\right)\right\} \quad (i=1,\ldots,M_0-1),$$

$$\text{and } T_{M_0}[l] \coloneqq \Re\left\{\sum_{k=(M_0-1)K_0}^{N-1} \frac{s^{(q)}[k]}{s^{(i)}[k]}\exp\left(j2\pi\frac{l}{N}k\right)\right\}.$$

The remainder of the proof follows along the same lines as Appendix II-C1.

D. PROOFS OF THEOREM 2, COROLLARY 3 AND COROLLARY 6

1) THEOREM 2

Let $\mathcal{S}$ denote the set of feasible realizations of the signal $s[n]$ $(n = 0, \ldots, N-1)$ (i.e., the codebook). In particular, let $a_0[n]$ denote the signal corresponding to the all-zero codeword (i.e., $\mathbf{c} = \mathbf{0} = \tilde{\mathbf{c}}$ in Fig. 3), which occurs with probability 2^{-m_sK} for linear codes. It is easily seen from (1) that when all the symbols in $s[n]$ are identical as in $a_0[n]$, then $|\chi(l; s[\cdot])| > u$ for $l \ll N$ and sufficiently small u. Thus, conditioning on $\mathcal{S}$, we have

$$\begin{aligned}\mathbb{P}(|\Re(\chi(l;s[\cdot]))|>u) &= \sum_{a[n]\in\mathcal{S}} \mathbb{1}(|\Re\{\chi(l;a[\cdot])\}|>u) \\ &\quad\times \mathbb{P}(s[n]=a[n]) \\ &\ge \mathbb{1}(|\Re\{\chi(l;a_0[\cdot])\}|>u) \\ &\quad\times \mathbb{P}(s[n]=a_0[n]) \\ &= \mathbb{P}(s[n]=a_0[n]) \\ &\quad\text{(for sufficiently small } u) \\ &= \exp(-(m_s\ln 2)rN). \end{aligned} \tag{56}$$

2) COROLLARY 3

For linear codes, the joint probability of the all-zero codeword for both $s^{(i)}[n]$ and $s^{(q)}[n]$ equals $2^{-(m_{s_i}K_i+m_{s_q}K_q)}$. The remainder of the proof follows along the same lines as Appendix II-D1.

3) COROLLARY 6

From (16), we observe that when all the symbols in $s^{(i)}[n]$ and $s^{(q)}[n]$ are identical – e.g., the all-zero codeword for both signals – then, $|\Re\{V^{(q\to i)}[0]\}| > u$, for sufficiently small u. The remainder of the proof follows along the same lines as Corollary 3 and Appendix II-D1.

E. PROOFS OF COROLLARIES 1, 4 AND 7

We begin with the proof of Corollary 1. For $l \neq 0$ and $u > 0$, we have from Theorem 1,

$$\begin{aligned} 0 &\le \lim_{N\to\infty} \mathbb{P}(|\Re\{\chi(l;s[\cdot])\}|>u) \\ &\le \lim_{N\to\infty} 2\exp(-O(rN)u^2) = 0. \end{aligned} \tag{57}$$

Thus, from (57) and Definition 3, it follows that $|\Re\{\chi(l; s[\cdot])\}|$ converges in distribution to the deterministic $\delta[l]$, as $N \to \infty$. The proofs of Corollaries 4 and 7 follow along similar lines from the results in Corollaries 2 and 5, respectively.

REFERENCES

[1] W. Zhou, R. Zhang, G. Chen, and W. Wu, "Integrated sensing and communication waveform design: A survey," *IEEE Open J. Commun. Soc.*, vol. 3, pp. 1930–1949, 2022.

[2] M. Alloulah and H. Huang, "Future millimeter-wave indoor systems: A blueprint for joint communication and sensing," *IEEE Comput.*, vol. 52, no. 7, pp. 16–24, Jul. 2019.

[3] Y. Ma, Z. Yuan, G. Yu, S. Xia, and L. Hu, "Waveform design using half-duplex devices for 6G joint communications and sensing," 2022, *arXiv:2201.00941*.

[4] M. Mert Şahin and H. Arslan, "Multi-functional coexistence of radar-sensing and communication waveforms," in *Proc. IEEE Veh. Technol. Conf. (VTC Fall)*, 2020, pp. 1–5.

[5] F. Dong, W. Wang, Z. Hu, and T. Hui, "Low-complexity beamformer design for joint radar and communications systems," *IEEE Commun. Lett.*, vol. 25, no. 1, pp. 259–263, Jan. 2021.

[6] M. Temiz, E. Alsusa, and M. W. Baidas, "Optimized precoders for massive MIMO OFDM dual radar-communication systems," *IEEE Trans. Commun.*, vol. 69, no. 7, pp. 4781–4794, Jul. 2021.

[7] J. Pritzker, J. Ward, and Y. C. Eldar, "Transmit precoder design approaches for dual-function radar-communication systems," Mar. 2022, *arXiv:2203.09571*.

[8] A. R. Chiriyath, B. Paul, and D. W. Bliss, "Radar-communications convergence: Coexistence, cooperation, and co-design," *IEEE Trans. Cogn. Commun. Netw.*, vol. 3, no. 1, pp. 1–12, Mar. 2017.

[9] S. H. Dokhanchi, M. R. B. Shankar, T. Stifter, and B. Ottersten, "OFDM-based automotive joint radar-communication system," in *Proc. IEEE Radar Conf.*, 2018, pp. 902–907.

[10] C. D. Ozkaptan, E. Ekici, O. Altintas, and C. Wang, "OFDM pilot-based radar for joint vehicular communication and radar systems," in *Proc. IEEE Veh. Netw. Conf. (VNC)*, 2018, pp. 1–8.

[11] C. D. Ozkaptan, E. Ekici, and O. Altintas, "Enabling communication via automotive radars: An adaptive joint waveform design approach," in *Proc. IEEE Conf. Comput. Commun. (INFOCOM)*, 2020, pp. 1409–1418.

[12] P. Kumari, J. Choi, N. González-Prelcic, and R. W. Heath, "IEEE 802.11ad-based radar: An approach to joint vehicular communication-radar system," *IEEE Trans. Veh. Technol.*, vol. 67, no. 4, pp. 3012–3027, Apr. 2018.

[13] E. Grossi, M. Lops, L. Venturino, and A. Zappone, "Opportunistic radar in IEEE 802.11ad networks," *IEEE Trans. Signal Process.*, vol. 66, no. 9, pp. 2441–2454, May 2018.

[14] H. Ajorloo, C. Sreenan, A. Loch, and J. Widmer, "On the feasibility of using IEEE 802.11ad mmWave for accurate object detection," in *Proc. 34th ACM/SIGAPP Symp. Appl. Comput.*, 2019, pp. 2406–2413.

[15] E. Grossi, M. Lops, A. M. Tulino, and L. Venturino, "Opportunistic sensing using mmWave communication signals: A subspace approach," *IEEE Trans. Wireless Commun.*, vol. 20, no. 7, pp. 4420–4434, Jul. 2021.

[16] T. Wild, V. Braun, and H. Viswanathan, "Joint design of communication and sensing for beyond 5G and 6G systems," *IEEE Access*, vol. 9, pp. 30845–30857, 2021.

[17] K. Wu, J. A. Zhang, X. Huang, and Y. J. Guo, "Joint communications and sensing employing multi- or single-carrier OFDM communication signals: A tutorial on sensing methods, recent progress and a novel design," *Sensors*, vol. 22, no. 4, p. 1613, Feb. 2022.

[18] F. Liu, C. Masouros, A. Li, J. Zhou, and L. Hanzo, "Simultaneous target detection and multi-user communications enabled by joint beamforming," in *Proc. IEEE Radar Conf.*, 2018, pp. 0089–0094.

[19] X. Liu, T. Huang, N. Shlezinger, Y. Liu, J. Zhou, and Y. C. Eldar, "Joint transmit beamforming for multiuser MIMO communications and MIMO radar," *IEEE Trans. Signal Process.*, vol. 68, pp. 3929–3944, Jun. 2020.

[20] C. Xu, B. Clerckx, and J. Zhang, "Multi-antenna joint radar and communications: Precoder optimization and weighted sum-rate vs probing power tradeoff," *IEEE Access*, vol. 8, pp. 173974–173982, 2020.

[21] C. Xu, B. Clerckx, S. Chen, Y. Mao, and J. Zhang, "Rate-splitting multiple access for multi-antenna joint radar and communications," *IEEE J. Sel. Topics Signal Process.*, vol. 15, no. 6, pp. 1332–1347, Nov. 2021.

[22] R. Cerna-Loli, O. Dizdar, and B. Clerckx, "A rate-splitting strategy to enable joint radar sensing and communication with partial CSIT," in *Proc. IEEE 22nd Int. Workshop Signal Process. Adv. Wireless Commun. (SPAWC)*, 2021, pp. 491–495.

[23] L. Chen, Z. Wang, Y. Du, Y. Chen, and F. R. Yu, "Generalized transceiver beamforming for DFRC with MIMO radar and MU-MIMO communication," *IEEE J. Sel. Areas Commun.*, vol. 40, no. 6, pp. 1795–1808, Jun. 2022.

[24] S. H. Dokhanchi, M. R. B. Shankar, M. Alaee-Kerahroodi, T. Stifter, and B. Ottersten, "Adaptive waveform design for automotive joint radar-communications system," in *Proc. IEEE Int. Conf. Acoust., Speech Signal Process. (ICASSP)*, 2019, pp. 4280–4284.

[25] Z. Xiao and Y. Zeng, "Waveform design and performance analysis for full-duplex integrated sensing and communication," *IEEE J. Sel. Areas Commun.*, vol. 40, no. 6, pp. 1823–1837, Jun. 2022.

[26] T. Mao, J. Chen, Q. Wang, C. Han, Z. Wang, and G. K. Karagiannidis, "Waveform design for joint sensing and communications in millimeter-wave and low terahertz bands," *IEEE Trans. Commun.*, vol. 70, no. 10, pp. 7023–7039, Oct. 2022.

[27] R. Zhang, B. Shim, W. Yuan, M. D. Renzo, X. Dang, and W. Wu, "Integrated sensing and communication waveform design with sparse vector coding: Low sidelobes and ultra reliability," *IEEE Trans. Veh. Technol.*, vol. 71, no. 4, pp. 4489–4494, Apr. 2022.

[28] "6G: The next hyper—Connected experience for all," Samsung Res., Suwon-Si, South Korea, White Paper, 2020. [Online]. Available: https://cdn.codeground.org/nsr/downloads/researchareas/6%20Vision.pdf

[29] Y. Zeng, Y. Ma, and S. Sun, "Joint radar-communication with cyclic prefixed single carrier waveforms," *IEEE Trans. Veh. Technol.*, vol. 69, no. 4, pp. 4069–4079, Apr. 2020.

[30] F. Liu, C. Masouros, A. P. Petropulu, H. Griffiths, and L. Hanzo, "Joint radar and communication design: Applications, state-of-the-art, and the road ahead," *IEEE Trans. Commun.*, vol. 68, no. 6, pp. 3834–3862, Jun. 2020.

[31] L. Sit, C. Sturm, T. Zwick, L. Reichardt, and W. Wiesbeck, "The OFDM joint radar-communication system: An overview," in *Proc. 3rd Int. Conf. Adv. Satell. Space Commun. SPACOMM*, Apr. 2011, pp. 1–6.

[32] C. B. Barneto et al., "Full-duplex OFDM radar with LTE and 5G NR waveforms: Challenges, solutions, and measurements," *IEEE Trans. Microw. Theory Tech.*, vol. 67, no. 10, pp. 4042–4054, Oct. 2019.

[33] J. Guan, A. Paidimarri, A. Valdes-Garcia, and B. Sadhu, "3D imaging using mmwave 5G signals," in *Proc. IEEE Radio Freq. Integr. Circuits Symp. (RFIC)*, 2020, pp. 147–150.

[34] S. D. Liyanaarachchi, C. B. Barneto, T. Riihonen, and M. Valkama, "Joint OFDM waveform design for communications and sensing convergence," in *Proc. IEEE Int. Conf. Commun. (ICC)*, 2020, pp. 1–6.

[35] L. Gaudio, M. Kobayashi, G. Caire, and G. Colavolpe, "On the effectiveness of OTFS for joint radar parameter estimation and communication," *IEEE Trans. Wireless Commun.*, vol. 19, no. 9, pp. 5951–5965, Sep. 2020.

[36] C. Sturm and W. Wiesbeck, "Waveform design and signal processing aspects for fusion of wireless communications and radar sensing," *Proc. IEEE*, vol. 99, no. 7, pp. 1236–1259, Jul. 2011.

[37] B. Bercu, B. Deylon, and E. Rio, *Concentration Inequalities for Sums and Martingales* (Briefs in Mathematics), 1st ed. Cham, Switzerland: Springer Int., 2015.

[38] S. Ling and C. Xing, *Coding Theory: A First Course*. Cambridge, U.K.: Cambridge Univ. Press, 2004.

[39] T. Mao, J. Chen, Q. Wang, C. Han, Z. Wang, and G. K. Karagiannidis, "Waveform design for joint sensing and communications in the terahertz band," 2021, *arXiv:2106.01549*.

[40] I. P. Eedara, A. Hassanien, M. G. Amin, and B. D. Rigling, "Ambiguity function analysis for dual-function radar communications using PSK signaling," in *Proc. 52nd Asilomar Conf. Signals, Syst., Comput.*, 2018, pp. 900–904.

[41] *5G NR—Physical Layer Procedures for Data, V15.3.0, Release 15*, 3GPP Standard TS 38.214, Oct. 2018.

[42] F. Uysal and S. Sanka, "Mitigation of automotive radar interference," in *Proc. IEEE Radar Conf. (RadarConf)*, Apr. 2018, pp. 405–410.

[43] G. Kim, J. Mun, and J. Lee, "A peer-to-peer interference analysis for automotive chirp sequence radars," *IEEE Trans. Veh. Technol.*, vol. 67, no. 9, pp. 8110–8117, Sep. 2018.